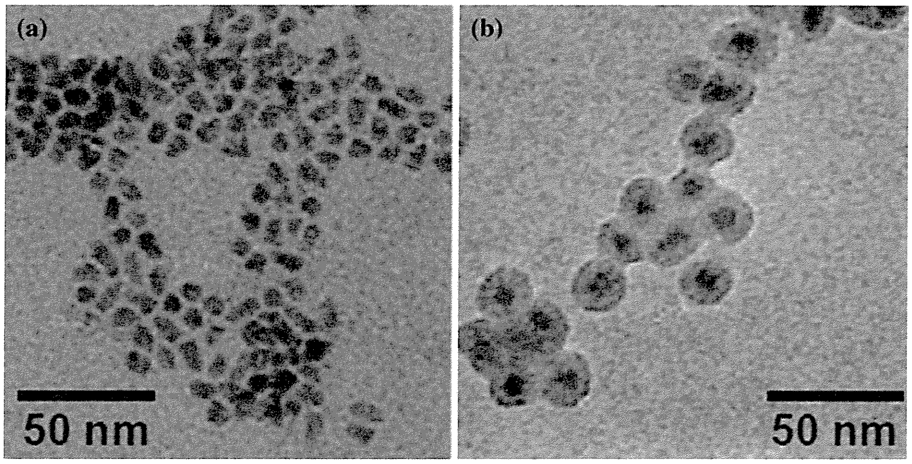

Fig. 1 TEM images of (**a**) QD nanoparticles and (**b**) QD/Si nanoparticles

Colloidal suspensions of QD/Si/Gd particles were washed by repeating centrifugation, removal of supernatant, addition of the water, and sonication over three times.

QD/Si/Gd/Si particles

Si-coating of the QD/Si/Gd particles was performed by the modified Stöber method in a 10-mL glass vessel under vigorous stirring. In each reaction, TEOS and 0.1 M aqueous NaOH solution were successively added to the QD/Si/Gd particle colloid solution at room temperature. The reaction time was 24 h. A total volume of the solution was 5 mL, and initial concentrations of QD, H_2O, NaOH, and TEOS were 3.2×10^{-9}, 5, 1×10^{-3}, and 5×10^{-4}–5×10^{-3} M, respectively. Colloidal suspensions of QD/Si/Gd/Si particles were washed by repeating centrifugation, removal of supernatant, addition of the water, and sonication over three times.

Characterization

Morphology of the particles was investigated by TEM. TEM was performed with a JEOL JEM-2000FX II microscope operating at 200 kV. Samples for TEM were prepared by dropping and evaporating the nanoparticle suspensions on a collodion-coated copper grid. Several hundred particle diameters in TEM images were measured to determine volume-averaged particle size, d_V, and standard deviation of particle size distribution, σ, defined by the following equations.

$$d_V = \left(\sum_i n_i d_i^3 \Big/ \sum_i n_i \right)^{1/3} \quad (1)$$

$$\sigma = \left(\sum_i (d_i - d_V)^2 \Big/ \sum_i n_i \right)^{1/2} \quad (2)$$

where n_i is the number of particles with a size of d_i.

Fluorescence intensity of each particle was measured with an optical system with confocal microscope, which was also used in our previous studies [48, 49]. The optical system for observation of fluorescence of particles consisted primarily of an epi-fluorescent microscope (IX-71, Olympus) with a 60× oil immersion objective lens (UPLSAPO; Olympus), a Nipkow disc-type confocal unit (CSU10, Yokogawa, Tokyo, Japan) and an electron multiplier type charge-coupled device camera (Ixon DV887, Andor, Belfast, Northern Ireland). One μL of sample was pipetted on to a glass slide (25 × 60 mm; Matsunami glass) and covered with a glass cover slip (24 × 32 mm; Matsunami glass). Particles were illuminated with a blue laser (488 nm, 50 mW, Spectra-Physics, CA, USA), and the laser-excited fluorescence was filtered with a 760–840 nm band-pass filter. The fluorescent images of particles were acquired by accumulating 100 images taken at an exposure time of 0.2 s and converted into AVI files. QDs possessing the same fluorescent wavelength are uniform in size, and its fluorescence is composed of fluorescent and non-fluorescent states called on- and off-states, respectively. This fluorescent property results in blinking of QDs. The mean time of the off-state during 20 s of observation was about 4 s and the calculated value of the standard error of the mean was very low. Therefore, based on an off-state time of 4 s, we selected ten single-particle QD. Their fluorescent intensity of 4 × 4 pixels (1.12 μm^2) during 20 s were averaged and calculated as gray value by Image J software (http://rsb.info.nih.gov/ij/).

Results and discussion

QD/Si/Gd particles

Gd-coating with NaOH-addition method and homogeneous precipitation method

Figure 2a shows TEM images of particles prepared with the NaOH-addition method. No Gd-coated core–shell

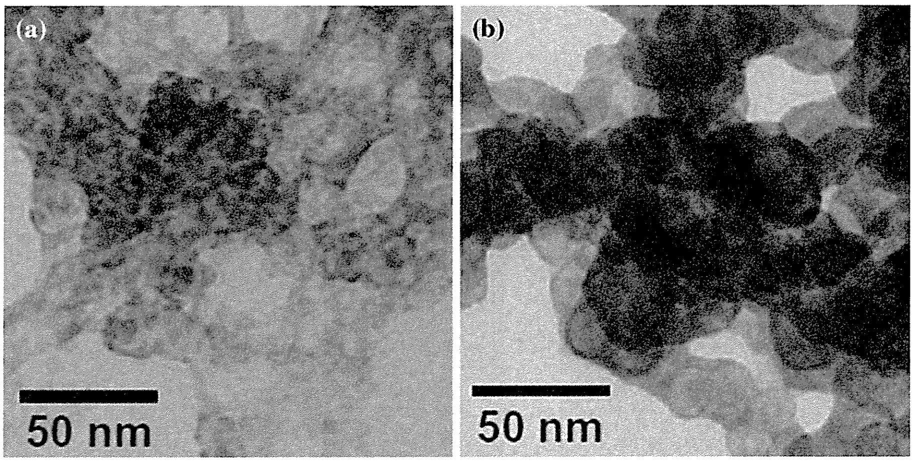

Fig. 2 TEM images of QD/Si nanoparticles after Gd-coating by (**a**) NaOH-addition method and (**b**) homogeneous precipitation method. Initial concentrations of QD and $Gd(NO_3)_3$ were 3.2×10^{-9} and 3×10^{-4} M, respectively. Urea concentration in the homogeneous precipitation method was 0.5 M

particles were produced. Instead, gel network of Gd formed, and the network appeared to incorporate the QD/Si particles. A local increase in pH of the colloid solution took place with the NaOH addition, which resulted in generation of large amount of Gd nuclei. The NaOH addition also provided a local increase in ionic strength of the solution close by the drops of NaOH aqueous solution. Since, an increase in the ionic strength compresses double layer on solid materials such as colloidal particles [50–52], the double layer repulsions both among the Gd nuclei and between the nuclei and the QD/Si particles were probably reduced with the NaOH addition. Thus, the aggregation of the Gd nuclei and the successive formation of their gel network took place simultaneously with the aggregation of the nuclei and the QD/Si particles. During the gel network formation, the QD/Si particles present in the colloid solution were probably incorporated with the network.

Figure 2b shows TEM images of particles prepared with the homogeneous precipitation method. The QD/Si particles were coated with Gd shell, though aggregation of the QD/Si/Gd particles was observed. Since, heating decomposed urea slowly, pH of the solution increased slowly and homogeneously, and then Gd nuclei was generated. The slow decomposition of urea resulted in not a fast but a slow increase in ionic strength of the solution. The slow increase in ionic strength controlled aggregation and growth of the Gd nuclei. Consequently, the Gd nuclei were deposited on the QD/Si particle surface. Accordingly, it was found that the homogeneous precipitation method was suitable to Gd-coating of the QD/Si particles, compared to the NaOH-addition method. Therefore, the homogeneous precipitation method was used for all subsequent experiments.

Effect of stabilizer

Figure 3 shows TEM images of QD/Si/Gd particles prepared with the homogeneous precipitation method using various stabilizers. In the cases of CTAB and SDS, though the QD/Si particles were coated with Gd shell, aggregation of the QD/Si/Gd particles was observed, which was similar to the case with no stabilizer (Fig. 2b). Because both CTAB and SDS are ionic surfactants, the addition of them may increase the ionic strength of solution. The increase in the ionic strength probably accelerated the aggregation of particles. The addition of PVP appeared to control the aggregation, i.e., quasi-perfect multilayered QD/Si/Gd

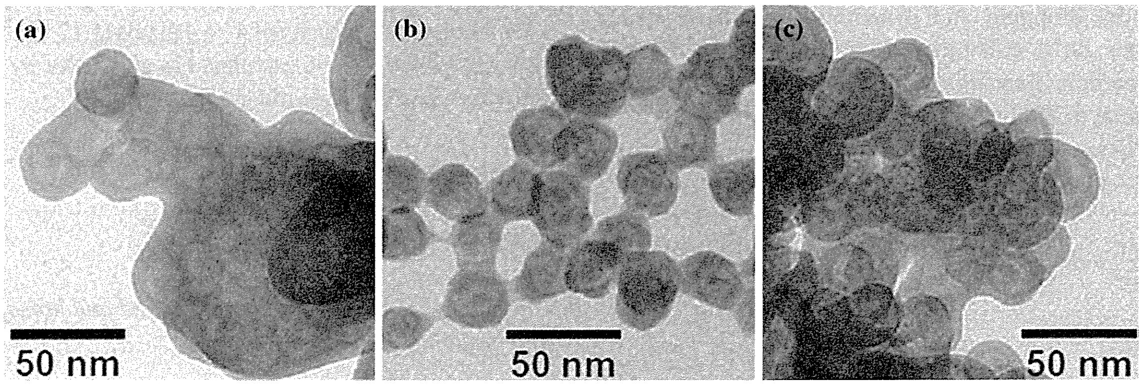

Fig. 3 TEM images of QD/Si/Gd nanoparticles prepared with homogeneous precipitation method using stabilizers of (**a**) CTAB, (**b**) PVP, and (**c**) SDS. Initial concentrations of QD, $Gd(NO_3)_3$, urea and stabilizer were 3.2×10^{-9}, 3×10^{-4}, 0.5 M, and 1 g/L, respectively

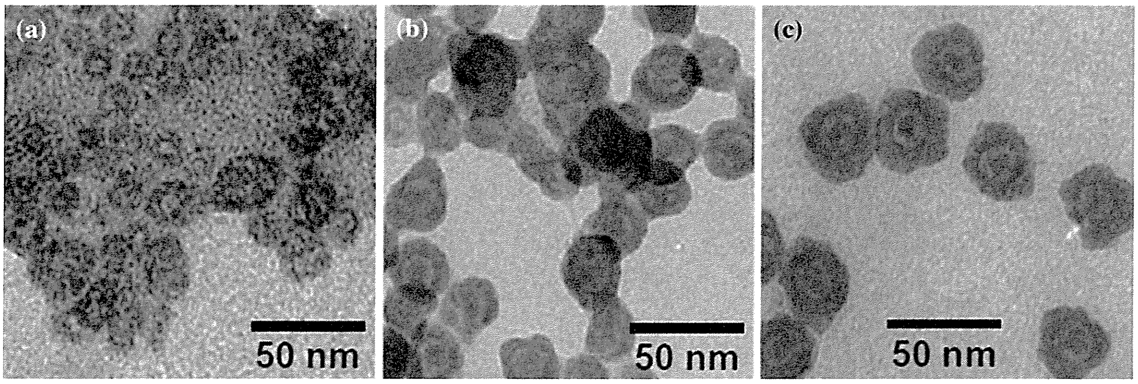

Fig. 4 TEM images of QD/Si/Gd nanoparticles prepared with homogeneous precipitation method at $Gd(NO_3)_3$ concentrations of (**a**) 3×10^{-5}, (**b**) 3×10^{-4}, and (**c**) 3×10^{-3} M. Initial concentrations of QD, urea, and PVP were 3.2×10^{-9}, 0.5 M, and 1 g/L, respectively

core–shell particles were produced with the PVP addition. Since, PVP is a polymer dispersant, the PVP addition probably did not provide remarkable change of ionic strength. Consequently, the particle aggregation became unpronounced. Therefore, the PVP was used for all subsequent experiments.

Effect of $Gd(NO_3)_3$ concentration

Figure 4 shows TEM images of QD/Si/Gd particles prepared with the homogeneous precipitation method at various $Gd(NO_3)_3$ concentrations. At a gadolinium concentration of 3×10^{-5} M, the QD/Si particles were Gd-coated, though the QD/Si/Gd particles were incorporated in gel network of Gd. An increase in the $Gd(NO_3)_3$ concentration to 3×10^{-4} M, quasi-perfect multilayered QD/Si/Gd particles were obtained, though the QD/Si/Gd particles appeared to aggregate. For a $Gd(NO_3)_3$ concentration as high as 3×10^{-3} M, the particle aggregation was almost prevented, and consequently the QD/Si/Gd particles became highly dispersed. The particle size was 42.5 ± 6.2 nm. Values of pHs of the particle colloid solutions at the $Gd(NO_3)_3$ concentrations of 3×10^{-5}, 3×10^{-4}, and 3×10^{-3} M were 8.1, 7.9, and 6.0, respectively. Because the QD/Si/Gd particle surface was covered with the Gd, properties of the QD/Si/Gd particle surface should be similar to those of the Gd particle surface. According to our previous study [53], Gd particles prepared with the homogeneous precipitation method had ζ-potentials of ca. 21, 24, and 37 mV at pHs of 8.1, 7.9, and 6.0, respectively. Accordingly, with the increase in the $Gd(NO_3)_3$ concentration, ζ-potential of QD/Si/Gd particles may have increased. Possibly, the increased ζ-potential at the high $Gd(NO_3)_3$ concentration provided large electric repulsion among the QD/Si/Gd particles, compared to the low $Gd(NO_3)_3$ concentration. Thus, the high-dispersed QD/Si/Gd particles were produced at the high $Gd(NO_3)_3$ concentration.

QD/Si/Gd/Si particles

Figure 5 shows TEM images of QD/Si/Gd/Si particles prepared at various TEOS concentrations. The QD/Si/Gd particles were coated with Si shell in all the TEOS concentrations examined. The particle sizes at 5×10^{-4}, 1×10^{-3}, and 5×10^{-3} M were 68.1 ± 7.9, 72.4 ± 8.7, 157.3 ± 27.7 nm, respectively. However, at the concentrations of 5×10^{-4} and 1×10^{-3} M, the QD/Si/Gd/Si particles aggregated and connected with other QD/Si/Gd/Si particles. Because Si particles have good stability as colloids, core particles should be colloidally stabilized by Si-coating. The Si shells were, however, so thin due to the low TEOS concentrations that the shells did not stabilize the QD/Si/Gd/Si particles colloidally. The increase in TEOS concentration to 5×10^{-3} M increased the Si shell thickness. The increase in thickness controlled the particle aggregation, and consequently high-dispersed QD/Si/Gd/Si particles were quasi-perfectly produced.

Fluorescence properties

Figure 6 shows fluorescence images of various particles on the glass plates. Bright spots show the fluorescence of QD contained in QD/Si/Gd/Si core–shell particles examined. Table 1 gives fluorescence intensities of various particles. As the layer number increased, fluorescence intensity of single particle tended to decrease. Excitation and emission of QD are probably prevented by optical absorption and scatter caused by Gd layer as SiO_2 layer does not affect fluorescent intensity of QD. Nevertheless, the QD/Si/Gd/Si particles revealed fluorescence with intensity as large as 67.5% of that of the QD particle with no shells.

Toward harmless fluorescence marker with MRI ability

Our previous study revealed that silica-coated Au nanoparticles revealed high contrast X-ray imaging [31]. A

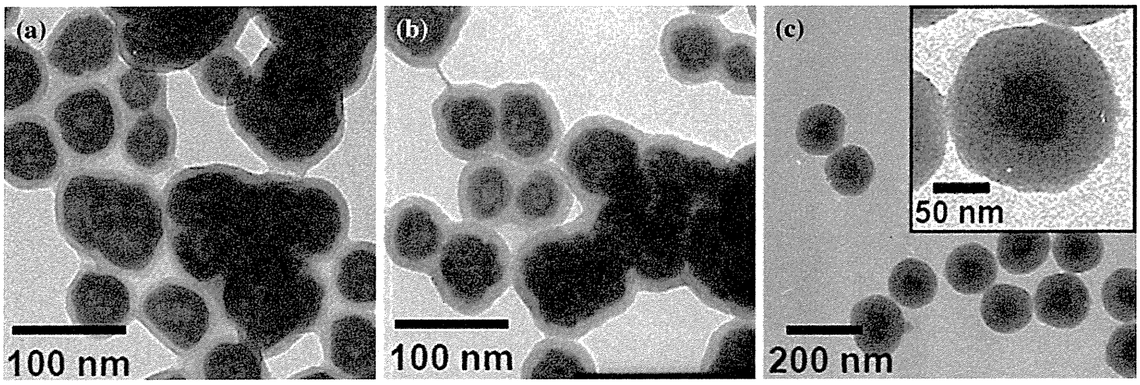

Fig. 5 TEM images of QD/Si/Gd/Si nanoparticles prepared at TEOS concentrations of (**a**) 5×10^{-4}, (**b**) 1×10^{-3}, and (**c**) 5×10^{-3} M. Initial concentrations of QD, $Gd(NO_3)_3$, urea, and PVP were 3.2×10^{-9}, 3×10^{-3}, 0.5 M, and 1 g/L, respectively

Fig. 6 Fluorescence images of (**a**) QD, (**b**) QD/Si, (**c**) QD/Si/Gd, and (**d**) QD/Si/Gd/Si particles

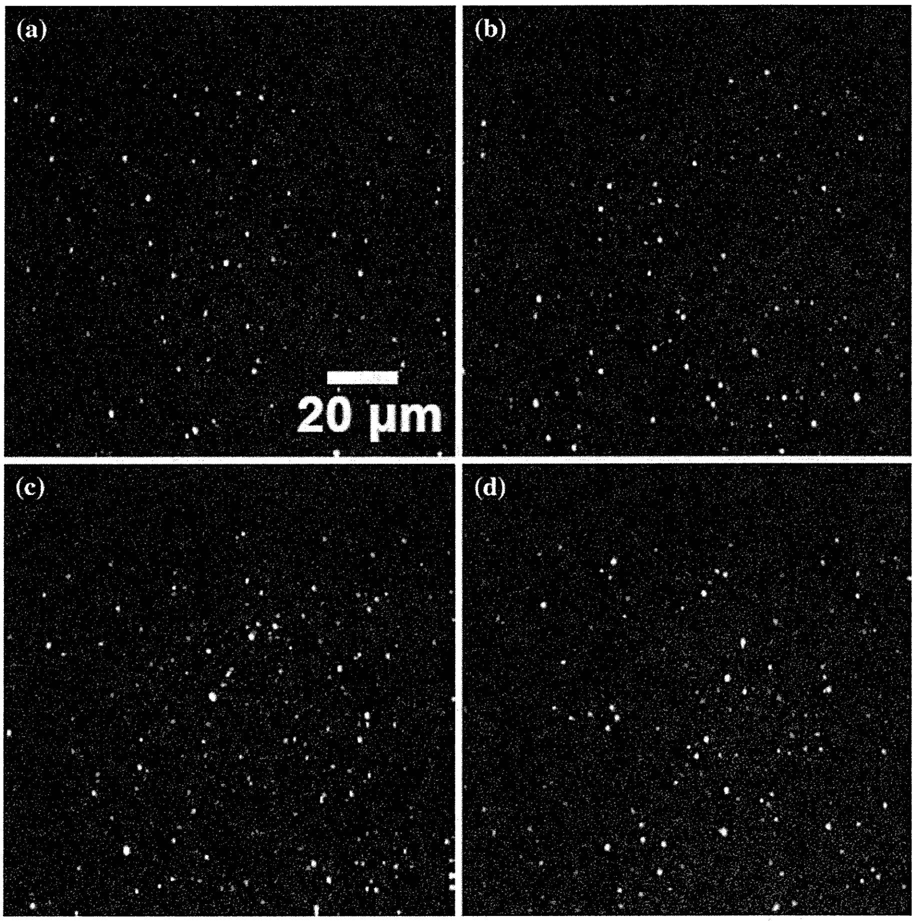

preliminary experiment confirmed that the silica-coated Au nanoparticles were nontoxic for mice. Therefore, the obtained multilayered core–shell particles will be harmless, because they have the outer silica shell. Our another previous study demonstrated that multilayered Si/Gd/Si core–shell particles showed MRI ability [54]. This result implies that the multi-layered core–shell particles obtained in this study will be functioned as an MRI contrast agent. This study indicated that the multi-layered core–shell particles emitted strong fluorescence. Consequently, it was summarized that the multi-layered core–shell particles were harmless to living bodies, and had dual functions of fluorescence marking and high contrast MRI.

Table 1 Relative fluorescent intensities of various particles

	QD	QD/Si	QD/Si/Gd	QD/Si/Gd/Si
Fluores. intensity	100	95.2	63.5	67.5

QD Fig. 1a, *QD/Si* Fig. 1b, *QD/Si/Gd* Fig. 4c, and *QD/Si/Gd/Si* Fig. 5a

Conclusions

This study proposed a method for producing multilayered QD/Si/Gd/Si core–shell particles. QD nanoparticles Si-coated with a modified Stöber method using TEOS and NaOH were coated with Gd shells by means of a homogeneous precipitation method. Si-coating of QD/Si/Gd core–shell particles was achieved by a sol–gel reaction of TEOS initiated by NaOH with the aid of stabilizer PVP. Fluorescence intensity of the multilayered QD/Si/Gd/Si particles was as large as 67.5% of that for the QD nanoparticles. Taking the results obtained in our previous studies and in this study, the multilayered QD/Si/Gd/Si core–shell particles can be used in the field of medical diagnosis as a harmless fluorescence marker with MRI ability.

Acknowledgement We express our thanks to Prof. T. Noguchi in College of Science of Ibaraki University, Japan for his help in TEM observation.

References

1. Ratzinger G, Agrawal P, Körner W, Lonkai J, Sanders HMHF, Terreno E, Wirth M, Strijkers GJ, Nicolay K, Gabor F (2010) Biomaterials 31:8716
2. Shiraishi K, Kawano K, Maitani Y, Yokoyama M (2010) J Control Release 148:160
3. Nwe K, Bernardo M, Regino CAS, Williams M, Brechbiel MW (2010) Bioorg Med Chem 18:5925
4. Bussi S, Fouillet X, Morisetti A (2007) Exp Toxicol Pathol 58:323
5. Gräfe JL, McNeill FE, Byun SH, Chettle DR, Noseworthy MD (2011) Appl Radiat Isot 69:105
6. Liu S, Zhang Z, Wang Y, Wang F, Han MY (2005) Talanta 67:456
7. Heitsch AT, Smith DK, Patel RN, Ress D, Korgel BA (2008) J Solid State Chem 181:1590
8. Lu P, Zhang JL, Liu YL, Sun DH, Liu GX, Hong GY, Ni JZ (2010) Talanta 82:450
9. Wang Y, Bai X, Liu T, Dong B, Xu L, Liu Q, Song H (2010) J Solid State Chem 183:2779
10. Wang L, Neoh KG, Kang ET, Shuter B (2011) Biomaterials 32:2166
11. Liu Z, Liu P, Liu C, Yao K, Ning Q, Xi D, Xu H (2007) J Mater Sci 42:5147. doi:10.1007/s10853-006-1284-0
12. Ghica C, Ionita P (2007) J Mater Sci 42:10058. doi:10.1007/s10853-007-1980-4
13. Wang X, Ji H, Zhang X, Zhang H, Yang X (2010) J Mater Sci 45:3981. doi:10.1007/s10853-010-4470-z
14. Liu G, Wu H, Zheng H, Tang L, Hu H, Yang H, Yang S (2011) J Mater Sci 46:5959. doi:10.1007/s10853-011-5551-3
15. Kobayashi Y, Horie M, Konno M, Rodríguez-González B, Liz-Marzán LM (2003) J Phys Chem B 107:7420
16. Mine E, Yamada A, Kobayashi Y, Konno M, Liz-Marzán LM (2003) J Colloid Interface Sci 264:385
17. Kobayashi Y, Misawa K, Kobayashi M, Takeda M, Konno M, Satake M, Kawazoe Y, Ohuchi N, Kasuya A (2004) Colloids Surf A 242:47
18. Kobayashi Y, Misawa K, Takeda M, Kobayashi M, Satake M, Kawazoe Y, Ohuchi N, Kasuya A, Konno M (2004) Colloids Surf A 251:197
19. Kobayashi Y, Katakami H, Mine E, Nagao D, Konno M, Liz-Marzán LM (2005) J Colloid Interface Sci 283:392
20. Mine E, Hirose M, Kubo M, Kobayashi Y, Nagao D, Konno M (2006) J Sol-Gel Sci Technol 38:91
21. Kobayashi Y, Horie M, Nagao D, Ando Y, Miyazaki T, Konno M (2006) Mater Lett 60:2046
22. Kobayashi Y, Misawa K, Takeda M, Ohuchi N, Kasuya A, Konno M (2007) Adv Mater Res 29–30:191
23. Kobayashi Y, Misawa K, Takeda M, Ohuchi N, Kasuya A, Konno M (2008) Mater Res Soc Symp Proc 1074E:I10
24. Kobayashi Y, Shimizu N, Misawa K, Takeda M, Ohuchi N, Kasuya A, Konno M (2008) Surf Eng 24:248
25. Kobayashi Y, Sakuraba T (2008) Colloids Surf A 317:756
26. Kobayashi Y, Kakinuma H, Nagao D, Ando Y, Miyazaki T, Konno M (2008) J Sol-Gel Sci Technol 47:16
27. Kobayashi Y, Kakinuma H, Nagao D, Ando Y, Miyazaki T, Konno M (2009) J Nanoparticle Res 11:1787
28. Kobayashi Y, Nozawa T, Nakagawa T, Gonda K, Takeda M, Ohuchi N, Kasuya A (2010) J Sol-Gel Sci Technol 55:79
29. Kobayashi Y, Minato M, Ihara K, Sato M, Suzuki N, Takeda M, Ohuchi N, Kasuya A (2010) J Nanosci Nanotechnol 10:7758
30. Kobayashi Y, Nozawa T, Takeda M, Ohuchi N, Kasuya A (2010) J Chem Eng Jpn 43:490
31. Kobayashi Y, Inose H, Nakagawa T, Gonda K, Takeda M, Ohuchi N, Kasuya A (2011) J Colloid Interface Sci 358:329
32. Kobayashi H, Hama Y, Koyama Y, Barrett T, Regino CAS, Urano Y, Choyke PL (2007) Nano Lett 7:1711
33. Xie J, Lee S, Chen X (2010) Adv Drug Deliv Rev 62:1064
34. Biju V, Mundayoor S, Omkumar RV, Anas A, Ishikawa M (2010) Biotechnol Adv 28:199
35. Brus LE (1984) J Chem Phys 80:4403
36. Vuu K, Xie J, McDonald MA, Bernardo M, Hunter F, Zhang Y, Li K, Bednarski M, Guccione S (2005) Bioconj Chem 16:995
37. Lin YS, Wu SH, Hung Y, Chou YH, Chang C, Lin ML, Tsai CP, Mou CY (2006) Chem Mater 18:5170
38. Guo J, Yang W, Deng Y, Wang C, Fu S (2005) Small 1:737
39. Selvan ST, Patra PK, Ang CY, Ying JY (2007) Angew Chem Int Ed 46:2448
40. Dubus S, Gravel JF, Drogoff BL, Nobert P, Veres T, Boudreau D (2006) Anal Chem 78:4457
41. Guo J, Yang W, Wang C, He J, Chen J (2006) Chem Mater 18:5554
42. Salgueiriño-Maceira V, Correa-Duarte MA (2007) Adv Mater 19:4131
43. Stöber W, Fink A, Bohn E (1968) J Colloid Interface Sci 26:62

44. Shimura N, Ogawa M (2007) J Mater Sci 42:5299. doi:10.1007/s10853-007-1771-y
45. Lu BW, Endo A, Inagi Y, Harada A, Ohmori T (2009) J Mater Sci 44:6463. doi:10.1007/s10853-009-3627-0
46. Mitchell SC, Zhang AQ (2001) Clin Chim Acta 312:107
47. Benigni R, Passerini L (2002) Mutat Res 511:191
48. Gonda K, Watanabe TM, Ohuchi N, Higuchi H (2010) J Biol Chem 285:2750
49. Hikage M, Gonda K, Takeda M, Kamei T, Kobayashi M, Kumasaka M, Watanabe M, Satomi S, Ohuchi N (2010) Nanotechnology 21:185103
50. Singh G, Song L (2007) J Membr Sci 303:112
51. Yilmaz H, Sato K, Watari K (2007) J Colloid Interface Sci 307:116
52. Li SZ, Xu RK (2008) Colloids Surf A 326:157
53. Morimoto H, Minato M, Nakagawa T, Sato M, Kobayashi Y, Gonda K, Takeda M, Ohuchi N, Suzuki N (2011) J Sol-Gel Sci Technol 59:650
54. Kobayashi Y, Imai J, Nagao D, Takeda M, Ohuchi N, Kasuya A, Konno M (2007) Colloids Surf A 308:14

Traffic 2011; 12: 1805–1820

doi:10.1111/j.1600-0854.2011.01279.x

Molecular Basis of Insulin-Responsive GLUT4 Trafficking Systems Revealed by Single Molecule Imaging

Hiroyasu Hatakeyama[1] and Makoto Kanzaki[1,2,*]

[1] Graduate School of Biomedical Engineering, Tohoku University, Sendai, Miyagi 980-8575, Japan
[2] Core Research for Evolutional Science and Technology, Japan Science and Technology Agency, Tokyo 102-0075, Japan
**Corresponding author: Makoto Kanzaki, kanzaki@bme.tohoku.ac.jp*

Development of a 'static retention' property of GLUT4, the insulin-responsive glucose transporter, has emerged as being essential for achieving its maximal insulin-induced surface exposure. Herein, employing quantum-dot-based nanometrology of intracellular GLUT4 behavior, we reveal the molecular basis of its systematization endowed upon adipogenic differentiation of 3T3L1 cells. Specifically, (i) the endosomes-to-*trans*-Golgi network (TGN) retrieval system specialized for GLUT4 develops in response to sortilin expression, which requires an intricately balanced interplay among retromers, golgin-97 and syntaxin-6, the housekeeping vesicle trafficking machinery. (ii) The Golgin-97-localizing subdomain of the differentiated TGN apparently serves as an intermediate transit route by which GLUT4 can further proceed to the stationary GLUT4 storage compartment. (iii) AS160/Tbc1d4 then renders the 'static retention' property insulin responsive, i.e. insulin liberates GLUT4 from the static state only in the presence of functional AS160/Tbc1d4. (iv) Moreover, sortilin malfunction and the resulting GLUT4 sorting defects along with retarded TGN function might be etiologically related to insulin resistance. Together, these observations provide a conceptual framework for understanding maturation/retardation of the insulin-responsive GLUT4 trafficking system that relies on the specialized subdomain of differentiated TGN.

Key words: sorting disorder, insulin resistance, quantum dot, retromer, sortilin, AS160/Tbc1d4, *trans*-Golgi network, TGN-golgin

Received 7 January 2011, revised and accepted for publication 8 September 2011, uncorrected manuscript published online 12 September 2011, published online 9 October 2011

Stimulus-dependent translocation of membrane proteins from intracellular pools to the cell surface is an important feature of cell physiology, and multiple examples of such processes have been identified including transporters and channels (1,2). One of the best-studied proteins is the insulin-responsive glucose transporter 4 (GLUT4), which is predominantly expressed in tissues displaying the highest levels of insulin-dependent glucose uptake such as adipocytes and muscle cells (3,4). This protein undergoes insulin-dependent translocation from an specialized intracellular pool, called the GLUT4 storage compartment, to the plasma membrane. This translocation is triggered by the activation of intracellular signaling cascades including phosphatidylinositol (PI) 3-kinase and Akt (5,6). As for 3T3L1 cells, the regulated membrane trafficking systems for GLUT4 are only present when these adipocytes are fully differentiated, while in undifferentiated fibroblasts which express no GLUT4, exogenously expressed GLUT4 shows no such trafficking behavior (7–9). Morphological and biochemical studies have indicated that, in adipocytes, GLUT4 is mainly localized in perinuclear tubulo-vesicular structures that lack conventional recycling endosomal markers, such as the transferrin receptor (TfR), but are enriched in insulin-responsive aminopeptidase (IRAP), sortilin and low-density lipoprotein receptor-related protein (LRP1) (10–13). However, details of the nature of this storage compartment remain elusive and the molecular basis of the unique GLUT4 trafficking system is essentially unknown. For example, it is clear that the insulin-responsive GLUT4 storage compartment is downstream from the endosomal recycling compartment (ERC) located distal to the early endosomes (11,14–17), but we do not know how endocytosed GLUT4 is efficiently segregated and targeted for the insulin-responsive GLUT4 storage compartment during/after passage through the ERC. Moreover, whether, and if so how, the *trans*-Golgi network (TGN) contributes to generating the insulin-responsive GLUT4 storage compartment also remains to be clarified, though multiple studies have demonstrated that the TGN apparently serves as a GLUT4 transit route to the GLUT4 storage compartment (14,16–20).

Using biochemical and molecular biological approaches, numerous elements involved in insulin-responsive GLUT4 trafficking systems have been identified, including sortilin and AS160/Tbc1d4, both of which are reportedly essential for generating the insulin-responsive property of GLUT4 (12,21). However, the molecular mechanisms by which these elements contribute to establishing the highly complex GLUT4 trafficking systems remain unknown because even their functional steps in the GLUT4 itinerary have yet to be specified, due at least in part to technical limitations in the quantitative investigation of intracellular GLUT4 behavior. We recently developed a novel method allowing us to directly measure individual intracellular

GLUT4 movements, employing Quantum dot (QD) fluorescent nanocrystals (8). A major breakthrough achieved by our novel approach was successful dissection of the intracellular GLUT4 trafficking process into discrete experimentally traceable steps, which revealed the existence of putative anchoring mechanisms statically retaining GLUT4 in its storage compartment in adipocytes, but not in undifferentiated fibroblasts. Furthermore, GLUT4 liberation from this static state appeared to be among the major functional aspects of insulin-mediated Akt activity in fully differentiated 3T3L1 adipocytes. Thus, although intensive efforts have been directed at elucidating the nature of the GLUT4 storage compartment employing various experimental approaches including morphological and biochemical analyses (7,11,22), our novel QD method revealed the stationary GLUT4 behavior observed only in differentiated 3T3L1 adipocytes to be an important kinetic characteristic of the GLUT4 storage compartment. This provides direct evidence that in the absence of insulin, 'static retention' (23), rather than 'dynamic retention' (24), is the major sequestration mechanism for GLUT4 in adipocytes (8). Importantly, we also demonstrated aberrant GLUT4 behavior including dysfunction of putative anchoring mechanisms under insulin-resistant conditions, a characteristic feature of type 2 diabetes, suggesting that proper formation of the stationary GLUT4 storage compartment is essential for appropriate insulin actions. Thus, in the present study, we attempted to further investigate the stationary GLUT4 compartment revealed by our QD-based nanometrology to gain a greater understanding of the molecular basis of the insulin-responsive GLUT4 trafficking systems endowed upon adipogenesis.

Results

Changes in GLUT4 behavior during 3T3L1 cell differentiation

With the QD-based single-molecule imaging of GLUT4 movement in 3T3L1 cells expressing myc-GLUT4-enhanced cyan fluorescent protein (ECFP), we successfully captured the movements of individual GLUT4 molecules (Figure 1A,B). These movements varied from molecule to molecule (Figure 1B). Based on the observed movements, we calculated two parameters representing individual GLUT4 movements, velocities and mean square displacement (MSD, Figure 1C). The time–course of velocities was first calculated for individual particle movements (Figure 1C, upper), and represented with the velocity distribution (Figure 1C, lower left). Rightward shift of the distribution represents an increase in the number of fast-moving molecules. MSD values were also calculated for individual particle movements and represented with MSD versus time plots (MSD curves, Figure 1C, lower right). The slope of the MSD curve is proportional to the diffusion coefficient of the molecules, i.e. mobile molecules have larger MSD curve slopes. In the present study, we evaluated GLUT4 behavior with mean velocity distributions and MSD curves within cells under the same treatment conditions as in our previous study (8). In some cases, we also show GLUT4 movements with representative diffusion coefficient maps (e.g. Figure 2D) constructed based on the diffusion coefficients of individual molecules estimated by fitting the first 10 time-points of the MSD curves (see *Methods*).

With this approach, we confirmed our previous data showing GLUT4 behavior in differentiated adipocytes to be quite restricted as compared to that in parental undifferentiated fibroblasts ectopically expressing myc-GLUT4-ECFP (8) (Figures 1C and S1A). For clear comparisons among treatment conditions, the velocity distributions were represented by the cumulative frequency (Figure 1C, *lines*) instead of the individual frequencies (Figure 1C, *dots*) utilized in our previous study (8). We further analyzed changes in GLUT4 behavior during adipogenic differentiation, and found that on differentiation day 3, the behavioral properties of GLUT4 were very similar to those in fully differentiated adipocytes (Figure 1D,E). Importantly, TfR, a recycling endosomal marker (7), did not display the static behavioral property typical of GLUT4 even after differentiation, though TfR movement also slowed slightly upon differentiation (Figure S1B,C). These observations indicate that GLUT4 and TfR have the same trafficking routes in fibroblasts, while upon differentiation, other systems come into existence that selectively recruit GLUT4, but not TfR, to the as yet poorly characterized stationary GLUT4 storage compartment existing only in adipocytes.

Sortilin is critical for generating static GLUT4 behavior

To identify factors possibly involved in the development of GLUT4-selective trafficking systems, we looked for a protein selectively restricting the movement of GLUT4, but not TfR, in undifferentiated fibroblasts. We focused on one of the major components of GLUT4-containing endosomes, sortilin, which has been proposed to be involved in the formation of insulin-responsive GLUT4 storage vesicles in adipocytes (9) and perhaps also in skeletal myocytes (25,26). Consistent with previous reports (12,27), sortilin expression was not detected in fibroblasts but was remarkably upregulated from day 3 of differentiation in 3T3L1 cells (Figure 2A), i.e. the same day that GLUT4 movement became significantly restricted (Figure 1E). With our single-molecule approach, we found that exogenous expression of sortilin/wild-type-enhanced yellow fluorescent protein (sortilin/WT-EYFP) in fibroblasts markedly reduced GLUT4 movement without altering TfR movement (Figures 2B,C and S1D). Diffusion coefficient maps, constructed based on the MSD curve of an individual molecule, clearly illustrated the restraining actions of sortilin on GLUT4 movement (Figure 2D). Although C-terminal modification (tagging) of sortilin reportedly abrogates binding with the Golgi-localizing, γ-adaptin ear homology domain, ADP ribosylation factor (ARF)-binding (GGA) proteins (28), we obtained the same results, in terms of the establishment of static GLUT4 behavior, when the cells expressed HA-sortilin lacking a tag at

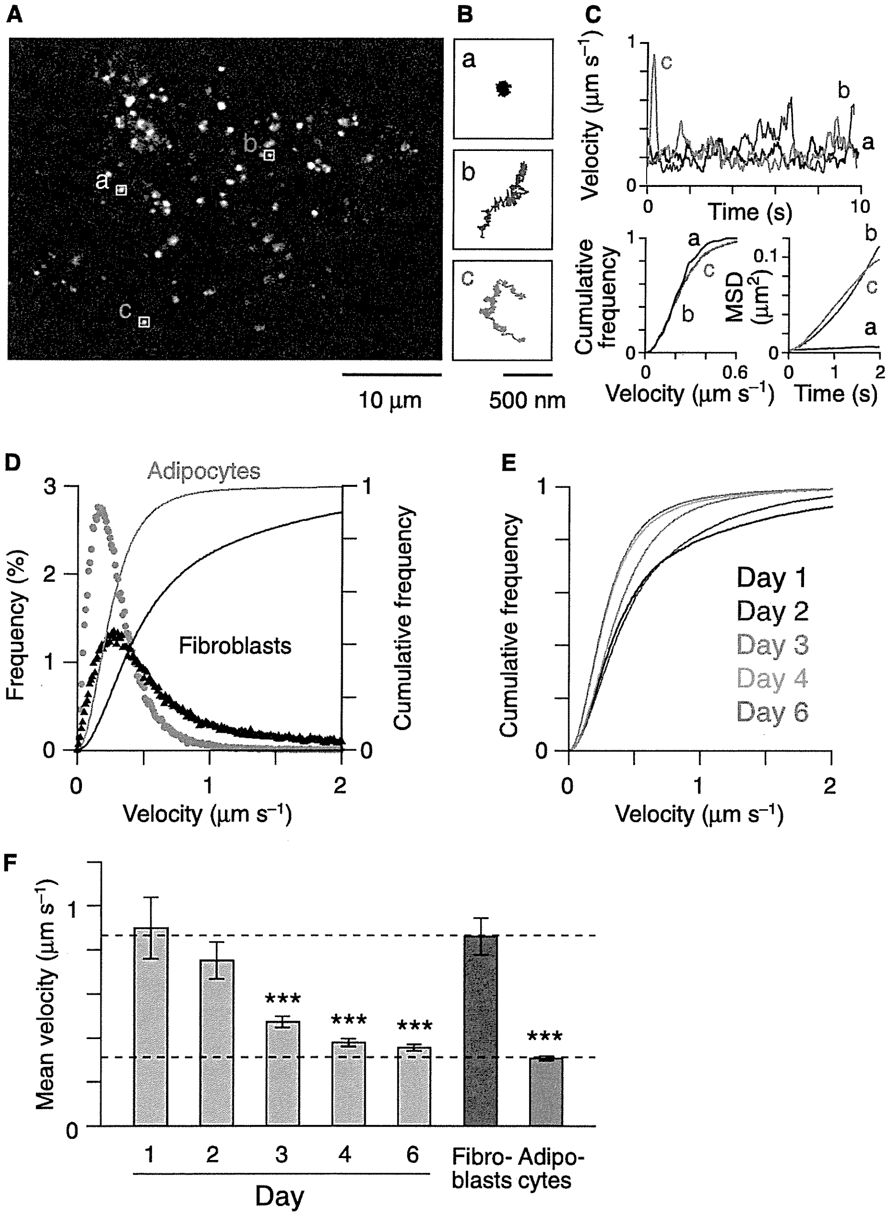

Figure 1: Changes in GLUT4 movement during 3T3L1 cell differentiation. A) Snapshot of QD fluorescence in 3T3L1 adipocytes. B) Trajectories of three particles shown in (A). C) Velocity versus time plots (upper), cumulative velocity distributions (lower left) and MSD curves (lower right) of three particles shown in (B). D) Mean velocity distributions of GLUT4 movement in undifferentiated fibroblasts (*black*) and differentiated adipocytes (*red*). Leftward shift of the distribution represents increases in the number of slow-moving molecules. Symbols and lines represent individual (*left axis*) and cumulative (*right axis*) velocity frequencies, respectively. The averaged values obtained from 17 fibroblasts, and from 11 adipocytes, were shown. Error bars are omitted for clarity. The mean velocities (±SD) were 0.31 ± 0.03 μm/s (adipocytes) and 0.86 ± 0.34 μm/s (fibroblasts, $p < 0.001$). E and F) Changes in velocity distributions (E) and mean velocities (F) during differentiation. E) Values obtained from undifferentiated fibroblasts (*blue*) and fully-differentiated adipocytes (*red*) are also shown for comparison. Data were obtained from 5–17 cells. ***$p < 0.001$ versus fibroblasts by Dunnett's multiple comparison.

the C-terminus (data not shown). The cation-independent mannose 6-phosphate receptor, another sorting receptor with a cytoplasmic sequence similar to that of sortilin (29), exerted no restrictive effect on GLUT4 movement (Figure 2B).

To ascertain whether endogenous sortilin is involved in the restricted GLUT4 movement endowed upon 3T3L1 cell differentiation, we applied siRNA-mediated knockdown of sortilin in fully differentiated adipocytes. Sortilin-targeted siRNA effectively reduced sortilin protein concomitantly with significant acceleration of GLUT4 movements associated with total disappearance of the stationary GLUT4 behavior (Figures 3A–C and S2A,B). In contrast, scrambled siRNA as a control had no such effects (Figure 3C). In addition, the static GLUT4 behavior was restored by sortilin rescue with siRNA-resistant sortilin/WT-EYFP (Supplemental Figure S2AC). Intriguingly, insulin stimulation failed to further accelerate GLUT4 movement in sortilin-depleted adipocytes (Figure 3D,E), despite insulin-responsive Akt phosphorylation being completely intact (Figure S2D). We also confirmed that rescue of sortilin expression restored insulin-responsive GLUT4 acceleration (data not shown).

These aberrant GLUT4 behavioral features in sortilin-depleted adipocytes are reminiscent of our previous observations in 3T3L1 adipocytes in an insulin-resistant state, elicited by chronic endothelin-1 (ET-1) treatment, conditions under which the stationary GLUT4 storage compartment largely disappeared (8). Therefore, we investigated sortilin expression in ET-1–treated

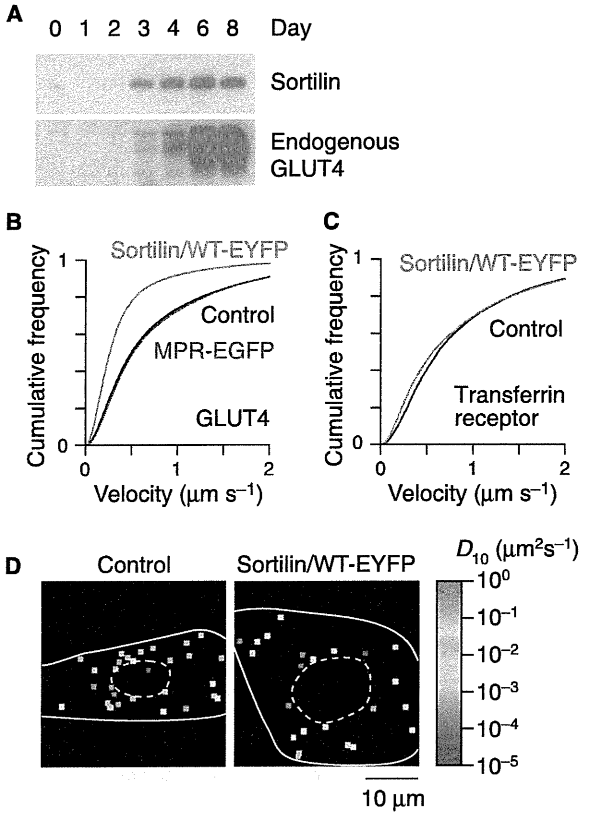

Figure 2: Involvement of sortilin in GLUT4-selective recruitment to anchoring sites. A) Western blotting of sortilin and endogenous GLUT4 expression during 3T3L1 cell differentiation. B) Velocity distributions of GLUT4 in control fibroblasts (*black*) or fibroblasts expressing sortilin/WT-EYFP (*red*) or mannose 6-phosphate receptor fused to enhanced green fluorescent protein (MPR-EGFP, *blue*). The mean velocities (±SD) were 0.83 ± 0.24 μm/s (control, $n = 51$), 0.46 ± 0.27 μm/s (sortilin/WT-EYFP, $n = 21$, $p < 0.001$) and 0.86 ± 0.27 μm/s (MPR-EGFP, $n = 13$, $p = 0.91$). Statistical analysis was performed using Dunnett's multiple comparison versus the control. C) Velocity distributions of TfR movement in control (*black*) and sortilin/WT-EYFP-expressing (*red*) fibroblasts. The mean velocities (±SD) were 0.89 ± 0.19 μm/s (control, $n = 10$) and 0.77 ± 0.13 μm/s (sortilin/WT-EYFP, $n = 5$, $p = 0.90$). D) Representative diffusion coefficient (D_{10}) maps in fibroblasts without (*left*) or with (*right*) sortilin/WT-EYFP expression. A pseudo-color coding, displayed on the right, is used to represent the diffusion coefficients of the molecules estimated by linear fitting of MSD curves versus time (see *Materials and Methods*). The mean MSD curves, calculated from all cells analyzed (control, $n = 51$; sortilin/WT-EYFP, $n = 21$), are shown in Figure S1D.

adipocytes, and found markedly reduced amount of sortilin protein in the insulin-resistant state (Figure 3F). These data suggest that aberrant GLUT4 behavior in ET-1–treated adipocytes results from reduced sortilin expression. We also observed restoration of static GLUT4 movement by sortilin overexpression in ET-1–treated adipocytes (unpublished observation), supporting our speculations.

Sortilin recruits GLUT4 to anchoring sites via retromer-mediated endosomes-to-TGN retrieval

To explore the precise molecular mechanisms underlying the development of the stationary GLUT4 storage compartment in response to sortilin expression, we attempted to identify the sorting motif(s) in the sortilin cytoplasmic tail (Figure 4A) that might directly or indirectly endow GLUT4 with its unique static behavior. To address this issue, we took advantage of undifferentiated fibroblasts, which readily allow detection of this restricted GLUT4 behavior, by exogenously expressing sortilin-EYFP (Figure 2B).

The potency of sortilin action in moving GLUT4 was significantly compromised when we mutated the sortilin cytoplasmic tail at either C^{783} or F^{787}LV, implicating both of these residues in retromer-mediated endosomes-to-TGN retrieval (29,30) (Figure 4B–D). However, no significant loss-of-function was detected when we mutated either $Y^{792}L^{795}$ or $L^{829}L^{830}$ (Figure 4B–D), implicating these residues in efficient endocytosis or GGA/AP1-mediated anterograde trafficking from TGN, respectively (28,29). Diffusion coefficient maps clearly illustrated the importance of sortilin retrograde trafficking involving its C^{783} and F^{787}LV residues and these mutants had no ability to restrict GLUT4 behavior (Figure 4E). Consistent with these observations, siRNA-mediated knockdown of a retromer complex component, Vps29 (31), abrogated the sortilin/WT-EYFP action on GLUT4 behavior (Figure 4F,G). Cells with knocked down Vps29 in the absence of sortilin showed no changes in GLUT4 behavior, and Vps29 rescue with siRNA-resistant HaloTag-Vps29 expression restored the actions of sortilin/WT-EYFP (data not shown). In addition, Vps29 knockdown in adipocytes also produced significant acceleration of GLUT4 movement associated with disappearance of its static behavior (data not shown). Note that the velocity distribution in Vps29-depleted cells was similar to that in fibroblasts expressing C^{783} and F^{787}LV mutants of sortilin hindering retrograde transport, which appears to be slightly different from that in intact fibroblasts expressing no sortilin (Figure 4B, control). These unidentified movements might reflect GLUT4 mistargeted to other compartments such as lysosomes, but not TGN, as a consequence of the impaired retrograde trafficking elicited either by the sortilin mutants or the Vps29 knockdown. Taken together, these observations indicate retromer-mediated retrograde transport of sortilin to be crucial to the static GLUT4 behavior, at least for internalized GLUT4, after cell surface exposure.

Intriguingly, despite the potency of the $Y^{792}L^{795}$ mutant in producing stationary GLUT4 behavior (Figure 4B), the $Y^{792}L^{795}$ mutant of sortilin, displaying slightly retarded endocytosis (29), appeared to be localized not only at cytoplasmic puncta including the perinuclear region but also at the plasma membrane (Figure 5). These results indicate that sortilin does not necessarily always need to be colocalized with GLUT4 to exert its ability to restrict GLUT4 behavior. Consistent with this notion, we unexpectedly found the luminal domain mutant of sortilin ($G^{334}E/A^{340}D$),

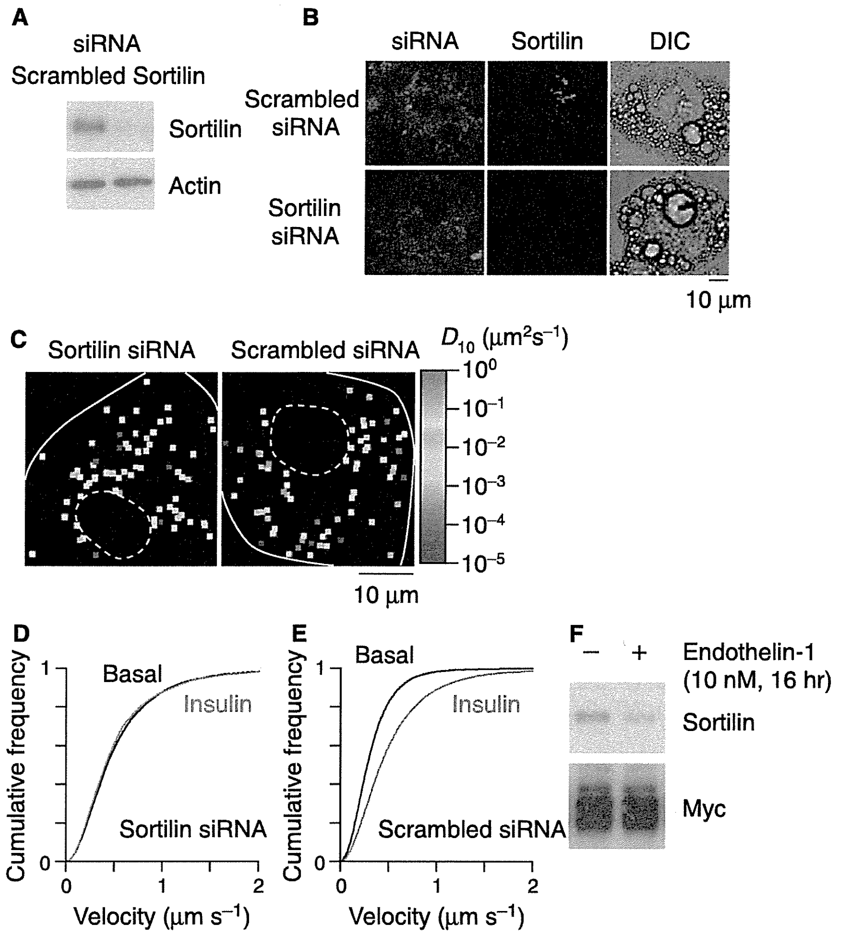

Figure 3: Knockdown of sortilin induces aberrant behavior of GLUT4. A and B) Western blotting (A) and immunofluorescence (B) of endogenous sortilin in differentiated adipocytes treated with siRNA. Cells were electroporated with Cy3-labeled sortilin or scrambled siRNA, and cultured for 48 h. C) Representative diffusion coefficient (D_{10}) maps of GLUT4 in adipocytes electroporated with sortilin (*left*) and scrambled (*right*) siRNA. Diffusion coefficients are represented by the pseudo-color coding displayed on the right. The mean MSD curves, calculated from all the cells analyzed (scrambled, $n = 16$; sortilin siRNA, $n = 21$), are shown in Figure S2. D and E) Velocity distributions of GLUT4 movement in adipocytes electroporated with sortilin (D) or scrambled (E) siRNA before (*black*) or after (*red*) stimulation with insulin (100 nM, 30 min). The mean velocities (±SD) in the basal states were 0.51 ± 0.10 μm/s (sortilin siRNA, $n = 21$) and 0.36 ± 0.04 μm/s (scrambled siRNA, $n = 16$, $p < 0.01$ versus sortilin siRNA), and those in the insulin-stimulated cells were 0.48 ± 0.12 μm/s (sortilin siRNA, $p = 0.30$ versus basal) and 0.57 ± 0.10 μm/s (Scrambled siRNA, $p < 0.01$ versus basal). F) Effects of endothelin-1 treatment (10 nM, 16 h) on sortilin and myc-GLUT4 expressions in adipocytes.

displaying a distinct localization pattern, to still have the capacity to establish static GLUT4 behavior (Figures 4D and 5). Collectively, these results suggest that sortilin itself does not contribute to anchoring GLUT4, but rather recruits GLUT4 to its anchoring sites via its retrograde transport property.

TGN-golgins are required for sortilin-induced formation of the stationary GLUT4 storage compartment

To clarify the destination of GLUT4 recruited by sortilin-mediated retrograde trafficking, we attempted to identify TGN-golgin(s) responsible for endosomes-to-TGN retrieval of GLUT4. The siRNA-mediated knockdown experiments in fully differentiated 3T3L1 adipocytes revealed that golgin-97 played important roles in proper recruitment of GLUT4 from endosomes to the TGN en route to the stationary storage compartment, since depletion of golgin-97 resulted in significant derangement (even complete loss) of static GLUT4 behavior (Figure 6A–C) despite endogenous sortilin levels remaining unchanged (Figure S3B). On the contrary, siRNA targeting golgin-245 minimally affected the sortilin-mediated development of static GLUT4 behavior, though a slight alteration in GLUT4 behavior (with MSD-t analysis) was detected with golgin-245 knockdown, and this was not observed in the control cells treated with scrambled siRNA (Figure 6A–C). Like sortilin expression, both TGN-golgins were up-regulated upon adipogenic differentiation, although a considerable amount of golgin-97, localized predominantly around the perinuclear region, was expressed even in undifferentiated fibroblasts (Figures 7A and 8A). As expected, in undifferentiated fibroblasts ectopically expressing both myc-GLUT4-ECFP and sortilin/WT-EYFP, siRNA-mediated knockdown of golgin-97 also aberrant sortilin-mediated static GLUT4 behavior (Figure 7B–D). The golgin-97 knockdown itself did not alter GLUT4 movements in control fibroblasts not expressing endogenous sortilin, and golgin-245 siRNA produced no significant changes in sortilin-mediated static GLUT4 behavior (data not shown). A crucial interplay between golgin-97 and sortilin-mediated retrograde trafficking of GLUT4 was further confirmed by immunofluorescent co-localization analysis of the endocytosed anti-Myc antibody (bound to myc-GLUT4-ECFP) with golgin-97 revealing that sortilin/WT, but neither the C^{783} mutant of sortilin nor the control efficiently induced their extensive co-localization and accumulation around the perinuclear region (Figure 8A). Intriguingly, the sortilin-mediated retrograde trafficking appeared to contribute to

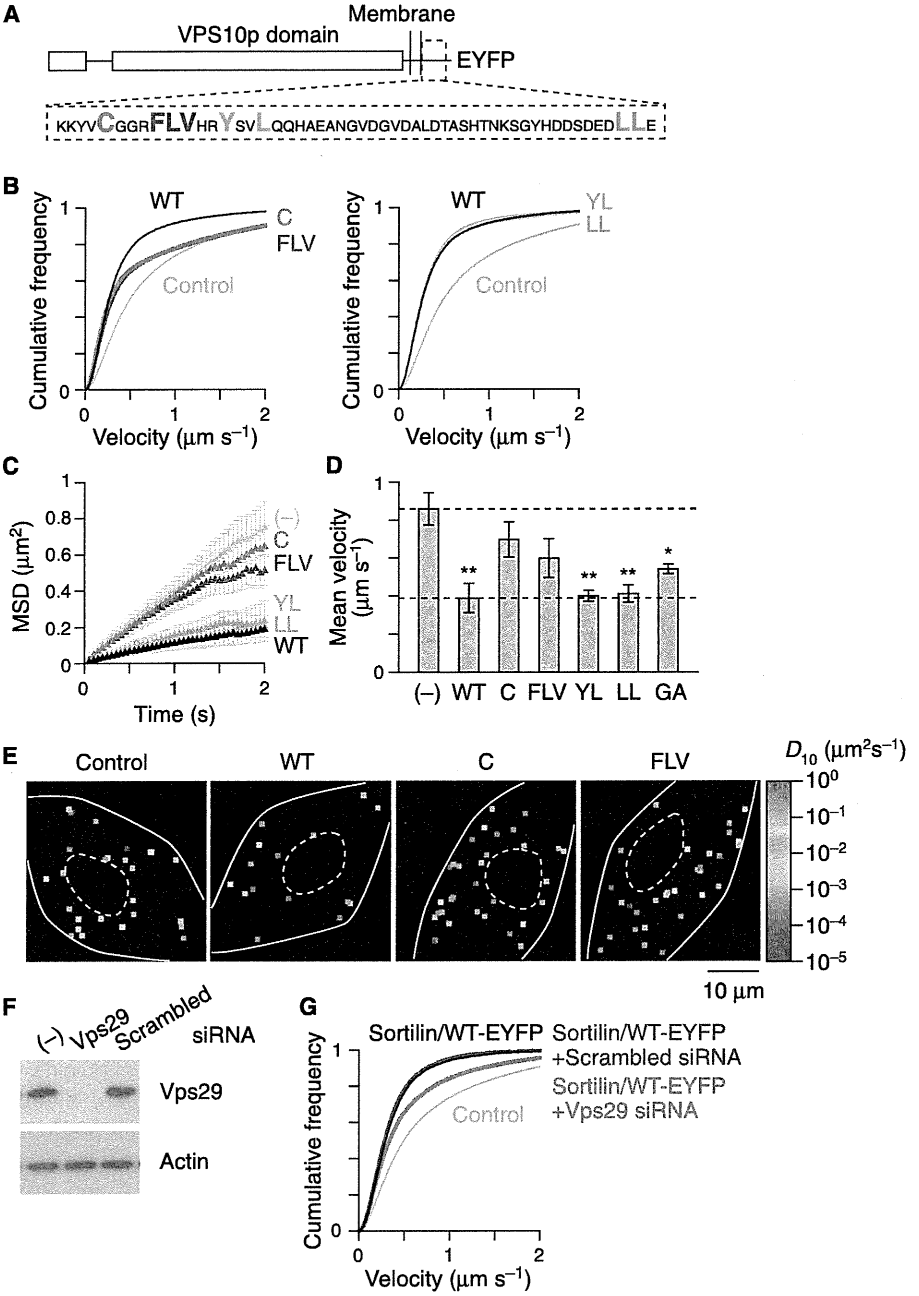

Figure 4: Involvement of retrograde transport of sortilin in restricted GLUT4 movement. A) Structure and amino acid sequence of cytosolic region of sortilin. Mutated amino acids are shown as large colored text. The mutations used were: C783S (C), F787A/L788A/V789A (FLV), Y792A/L795A (YL) and L829A/L830A (LL). B–D) Velocity distributions (B), mean MSD curves (C) and mean velocities (D) of GLUT4 movement in fibroblasts expressing the indicated mutants of sortilin-EYFP. The distributions in control (*gray*) and sortilin/WT-EYFP-expressing (*black*) cells are also shown for comparison. In (C) and (D), data are presented as means ± SEM. Statistical analysis was performed with Dunnett's multiple comparison versus control. $^*p < 0.05$, $^{**}p < 0.01$. GA represents the G334E/A340D mutant of sortilin-EYFP. E) Representative diffusion coefficient (D_{10}) maps of GLUT4 in fibroblasts expressing the indicated mutants of sortilin-EYFP. Diffusion coefficients are represented by the pseudo-color coding displayed on the right. F) Western blotting of Vps29 in fibroblasts treated with the indicated siRNA. G) Velocity distributions of GLUT4 movement in fibroblasts transfected with sortilin/WT-EYFP + Vps29 siRNA (*red*) and sortilin/WT-EYFP + scrambled siRNA (*blue*). The distributions in control (*gray*) and sortilin/WT-EYFP-expressing (*black*) cells are also shown for comparison. The mean velocities (±SD) were 0.74 ± 0.21 μm/s (control, $n = 13$), 0.40 ± 0.10 μm/s (sortilin/WT-EYFP, $n = 17$, $p < 0.001$), 0.62 ± 0.12 μm/s (sortilin/WT-EYFP + Vps29 siRNA, $n = 14$, $p = 0.058$) and 0.38 ± 0.08 μm/s (Sortilin/WT-EYFP + scrambled siRNA, $n = 13$, $p < 0.001$). Statistical analysis was performed using Dunnett's multiple comparison versus the control.

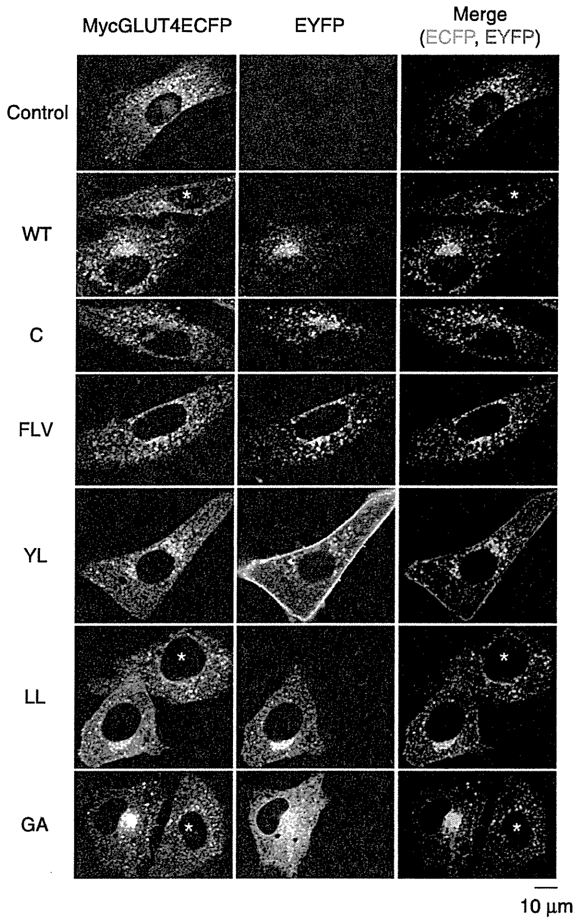

Figure 5: Fluorescent images of myc-GLUT4-ECFP and sortilin-EYFP mutants in fibroblasts. Expression vectors containing cDNA encoding either wild-type sortilin-EYFP (WT) or its mutant version were transfected into 3T3L1 fibroblasts expressing myc-GLUT4-ECFP and their localizations were visualized under a conventional confocal laser-scanning microscope. The sortilin mutants used were: C783S (C), F787A/L788A/V789A (FLV), Y792A/L795A (YL), L829A/L830A (LL) and G334E/A340D (GA). Images are representative fields-of-view from at least three independent experiments. Asterisks represent the cells with no detectable expression of sortilin-EYFP.

redistribution not only of myc-GLUT4-ECFP, but also soluble n-ethylmaleimide-sensitive factor (NSF)-attachment protein receptor (SNARE) proteins including syntaxin 6 and Vti1a, to the perinuclear region (Figure 8B). In addition, siRNA-mediated knockdown of golgin-97 in fully differentiated adipocytes similarly resulted in a dispersed redistribution of syntaxin 6 without reducing sortilin contents (Figure S3A,B), while golgin-245 knockdown had no effect (Figure S3C), as in previous reports (32,33). Taken together, these observations indicate that golgin-97 plays an essential role in sortilin-mediated development of the stationary GLUT4 storage compartment along with redistribution of syntaxin 6 to the perinuclear region.

Both sortilin and AS160 are required for insulin-responsive GLUT4 release from the stationary GLUT4 storage compartment

Finally, we examined the insulin responsiveness of stationary GLUT4 storage compartments artificially established by expressing sortilin in fibroblasts. Unlike differentiated adipocytes displaying efficient insulin-induced GLUT4 liberation (8), insulin stimulation failed to release GLUT4 from its static state in fibroblasts expressing sortilin/WT-EYFP (Figure 9A,B), suggesting an additional component(s) to be required to render the stationary GLUT4 storage compartment insulin responsive. We found that insulin-induced liberation of GLUT4 additionally required AS160/Tbc1d4, a RabGAP, which appeared also to be upregulated upon adipogenic differentiation (Figures 9C,D and S4A–D). Treatment with wortmannin, a PI 3-kinase inhibitor (34), or expression of the $T^{642}A$ mutant of AS160, an important Akt (35) phosphorylation site, completely abolished the insulin effect (Figure S4E–H), consistent with our previous observations in adipocytes (8). Importantly, expression of only HaloTag-AS160 produced neither the ability to endow static GLUT4 behavior nor changes in any features of GLUT4 movement regardless of insulin stimulation (Figure 9E,F). To ascertain the actions of endogenous AS160 in adipocytes, we applied siRNA-mediated knockdown of AS160 in fully differentiated adipocytes. AS160-targeted siRNA effectively reduced AS160 protein (Figure S5A). As expected, insulin essentially lost the ability to trigger the release GLUT4 from its static sate in AS160-depleted adipocytes (Figure S5D,E). It should be noted that in AS160-depleted adipocytes we detected very subtle but statistically significant alterations in basal GLUT4 behavior (Figure S5F,G), suggesting possible involvement of AS160 in the basal GLUT4 retention property of adipocytes.

To determine the relationships between intracellular GLUT4 movements and amount of surface GLUT4, we performed a myc-GLUT4 translocation assay in fibroblasts expressing myc-GLUT4-enhanced green fluorescent protein (EGFP) in the presence or absence of sortilin and AS160, and obtained results consistent with those based on our single-molecule analysis of GLUT4 behavior (data not shown), sortilin significantly reduced basal surface GLUT4, but insulin failed to induce translocation to the cell surface with sortilin expression alone. In contrast, in the presence of both sortilin and AS160, insulin markedly stimulated translocation. These observations indicate that liberation from anchoring sites is critical to cell surface exposure of GLUT4.

Discussion

Despite major advances in specifying the molecular elements on GLUT4-containing vesicles (12,13,36), the most fundamental unanswered question remains, i.e. how is the insulin-responsive GLUT4 trafficking system established upon adipogenic differentiation? Employing our QD-based

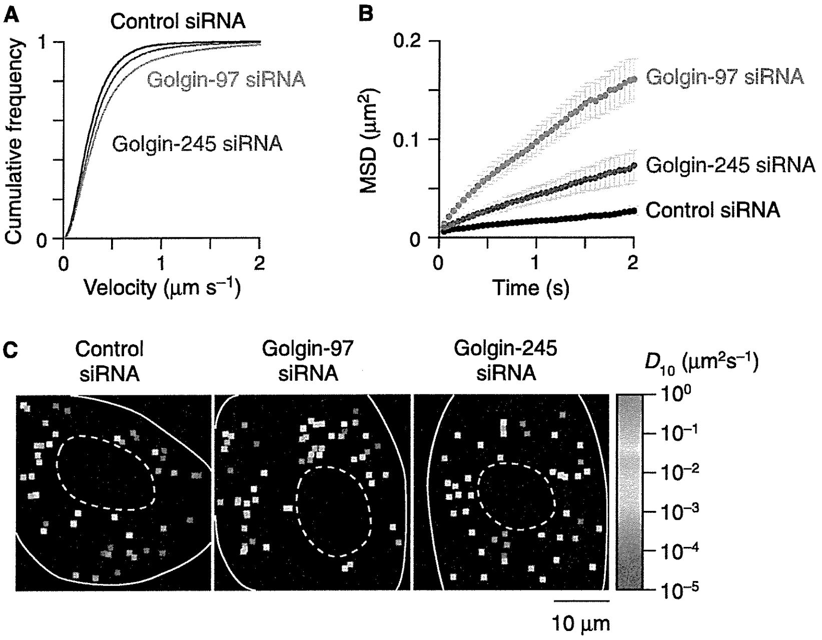

Figure 6: Involvement of TGN-golgins in restricted GLUT4 movement in adipocytes. A and B) Velocity distributions (A) and MSD curves (B) of GLUT4 movements in adipocytes electroporated with control (*black*), golgin-97 (*red*) or golgin-245 (*blue*) siRNAs. The mean velocities (±SD) were 0.29 ± 0.02 μm/s (control siRNA, $n = 8$), 0.45 ± 0.08 μm/s (golgin-97 siRNA, $n = 20$, $p < 0.001$) and 0.34 ± 0.02 μm/s (golgin-245 siRNA, $n = 12$, $p = 0.064$). Statistical analysis was performed with Dunnett's multiple comparison versus control siRNA. C) Representative diffusion coefficient (D_{10}) maps of GLUT4 in adipocytes electroporated with control (*left*), golgin-97 (*middle*) or golgin-245 (*right*) siRNAs.

nanometrology of GLUT4 behavior (8), we revealed a developmental network for the stationary GLUT4 storage compartment that fully accounts for insulin-responsive liberation from its static state. This observation unmasks the crucial participation of differentiated TGN, established in response to the sortilin-mediated retrograde trafficking property, which apparently relies on the Golgi apparatus, possessing a highly organized 'static' architecture but serving as the core of the 'dynamic' secretory pathway (Figure 10).

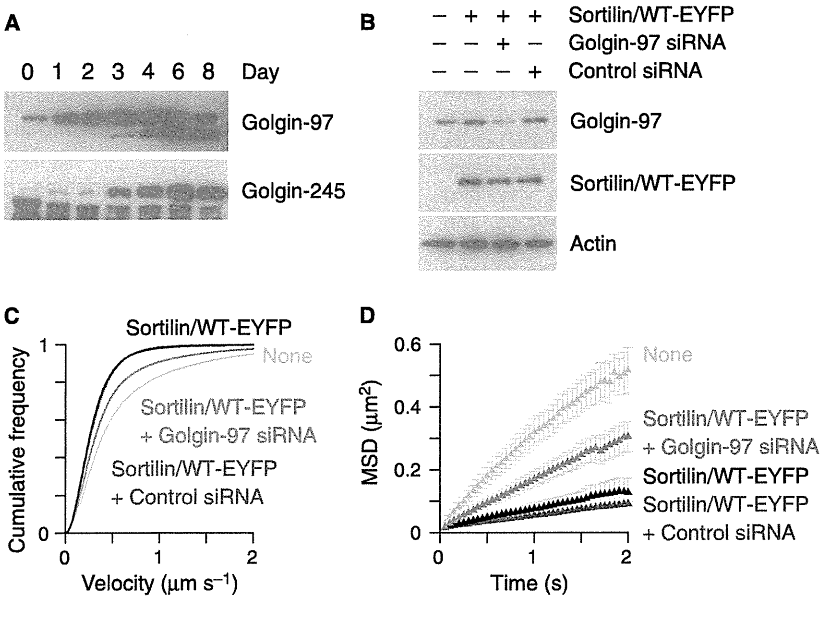

Figure 7: Effects of TGN-golgins on restricted GLUT4 movement in fibroblasts. A) Western blotting of golgin-97 and golgin-245 during 3T3L1 cell differentiation. B) Western blotting of golgin-97, sortilin and actin in fibroblasts transfected with the indicated DNA and/or siRNA. C and D) Velocity distributions (C) and mean MSD curves (D) of GLUT4 movement in control fibroblasts ('None', *gray*) or fibroblasts transfected with sortilin/WT-EYFP (*black*), sortilin/WT-EYFP + golgin-97 siRNA (*red*) and sortilin/WT-EYFP + control siRNA (*blue*). The mean velocities (±SD) were 0.66 ± 0.20 μm/s (control, $n = 8$), 0.32 ± 0.05 μm/s (sortilin/WT-EYFP, $n = 9$, $p < 0.001$ versus control), 0.46 ± 0.08 μm/s (sortilin/WT-EYFP + golgin-97 siRNA, $n = 10$, $p < 0.01$ versus sortilin/WT-EYFP) and 0.31 ± 0.02 μm/s (sortilin/WT-EYFP + control siRNA, $n = 7$, $p = 0.99$ versus sortilin/WT-EYFP). Statistical analysis was performed with Tukey's multiple comparison.

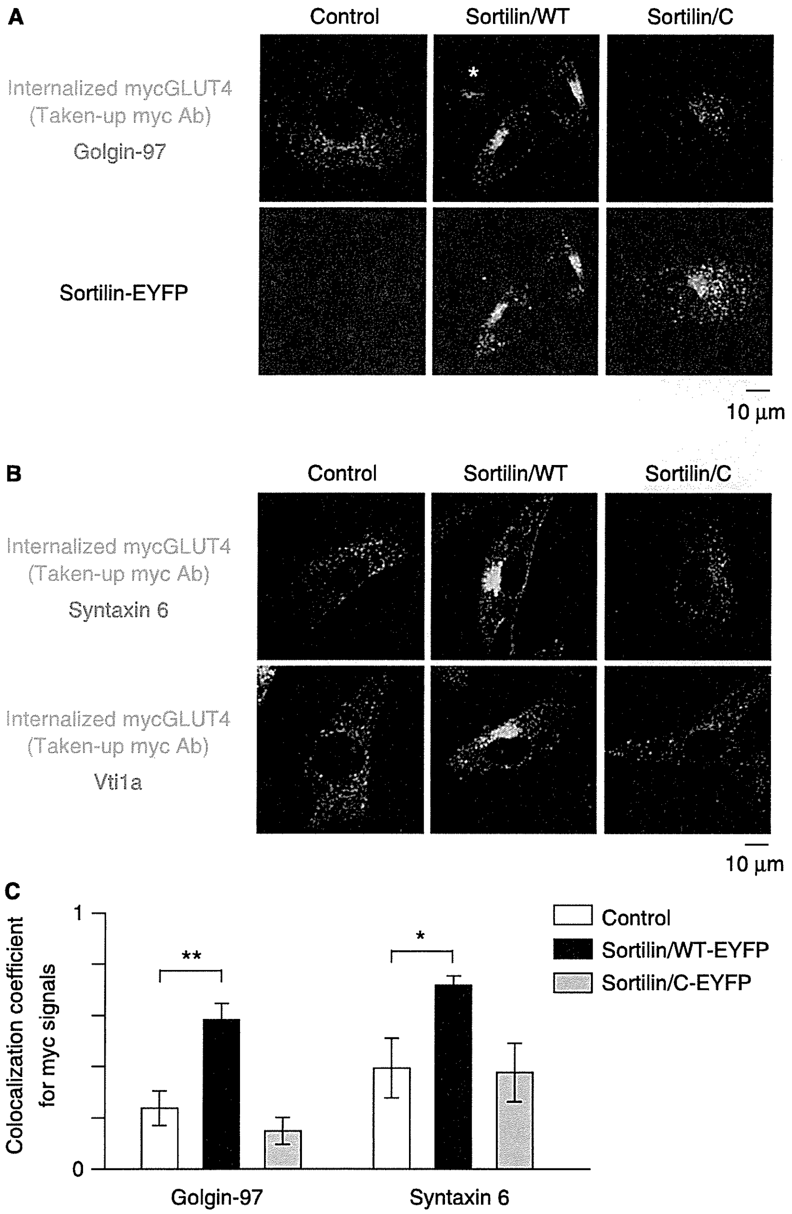

Figure 8: Involvement of retrograde transport of sortilin in localization of internalized myc-GLUT4-ECFP, syntaxin 6 and Vti1a. A) Immunofluorescent images of internalized myc-GLUT4-ECFP stained with taken-up anti-Myc Ab (top, *green*), golgin-97 (top, *red*) and EYFP (bottom) in control fibroblasts (left) or fibroblasts expressing sortilin/WT-EYFP (center) or sortilin/C-EYFP (right). Asterisks represent cells with no detectable expression of sortilin-EYFP. B) Immunofluorescent images of internalized myc-GLUT4-ECFP stained with taken-up anti-Myc Ab (*green*) and syntaxin 6 (top, *red*) or Vti1a (bottom, *red*) in fibroblasts. C) Quantification of the co-localization of internalized myc-GLUT4-ECFP stained with taken-up anti-Myc Ab with golgin-97 or syntaxin 6. Data were obtained from eight cells, and are presented as means ± SEM. $^*p < 0.05$, $^{**}p < 0.01$ by Dunnett's multiple comparison versus control.

In the present study, we focused on the establishment of stationary GLUT4 behavior as assessed by QD-based GLUT4 movements and revealed a sortilin-dependent interaction of endocytosed GLUT4 with the specialized subdomain of TGN. This interaction generates the 'static GLUT4 retention' compartment that further requires AS160 to render its static property insulin responsive (Figures 9 and S4). In excellent agreement with our findings, it has been proposed that TGN interacts with recycling endosomes to generate insulin-responsive GLUT4 storage compartments (16,19,20,23,37). However, a small but significant fraction of GLUT4 exists as a mobile phase even in differentiated 3T3L1 adipocytes under basal conditions (8), which may represent GLUT4 engaging in the general recycling pathway (7) and/or contributing to the assemblage of 'dynamic GLUT4 retention' (24,38–41). Thus, our data do not rule out the possibility that a subpopulation of GLUT4 may travel through only endosomal compartment(s), i.e. not through TGN, from the ERC destined for a distinct insulin-responsive GLUT4 storage pool exhibiting no static behavior. However, it merits emphasis that our quantitative analysis indicates stationary GLUT4 to be predominant in fully differentiated 3T3L1 adipocytes, but not in immature pre-adipocytes (fibroblastic cells).

A very striking observation made in this quantitative study is that changes in sortilin expression, whether developmental, experimental or pathological, markedly alter intracellular trafficking activities of GLUT4 (Figures 1–3,

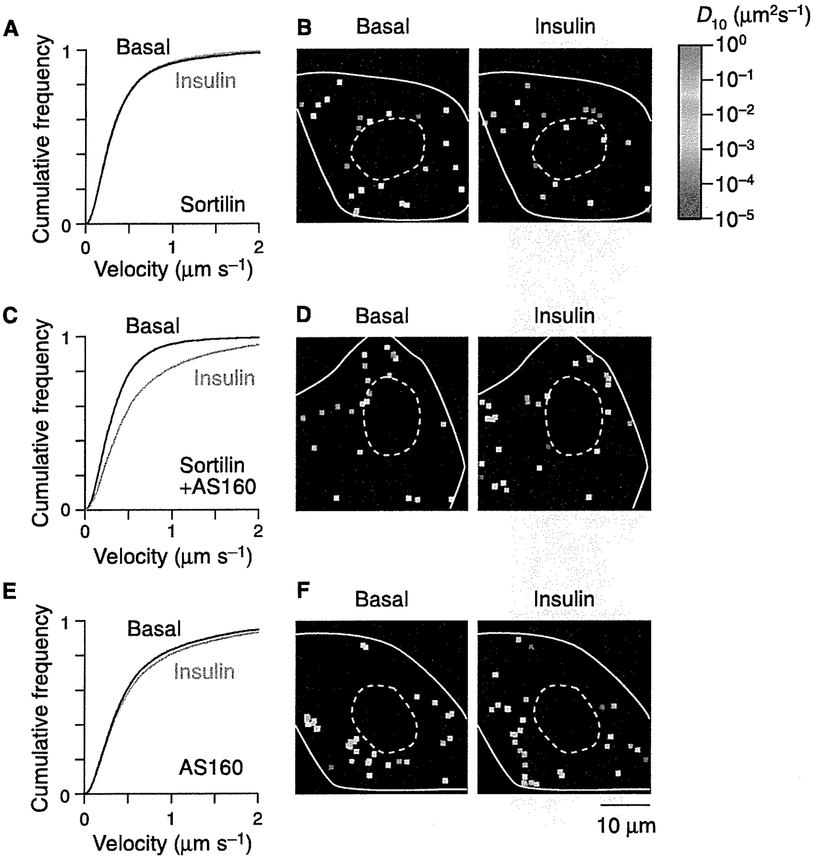

Figure 9: Involvement of both sortilin and AS160 in the liberation of GLUT4. Velocity distributions (A, C and E) and representative diffusion coefficient (D_{10}) maps (B, D and F) of fibroblasts expressing sortilin/WT-EYFP (A and B), sortilin/WT-EYFP + HaloTag-AS160 (C and D) and HaloTag-AS160 (E and F). Movements were analyzed in a cell before (*black*) and after (*red*) insulin stimulation (100 nM, 30 min). The mean velocities (±SD) were as follows. Sortilin/WT-EYFP ($n = 5$); basal: 0.43 ± 0.06 µm/s, insulin: 0.42 ± 0.17 µm/s ($p = 0.53$), sortilin/WT-EYFP + HaloTag-AS160 ($n = 15$; basal: 0.46 ± 0.10 µm/s, insulin: 0.67 ± 0.13 µm/s ($p < 0.05$), HaloTag-AS160 ($n = 4$); basal: 0.79 ± 0.06 µm/s, insulin: 0.72 ± 0.13 µm/s ($p = 0.31$). Diffusion coefficients are represented by the pseudo-color coding displayed on the right. The mean MSD curves, calculated from all cells analyzed, are shown in Figure S4.

S1 and S2). Specifically, sortilin is critical for establishing the development-dependent stationary storage compartment (Figures 1 and 2), and this process is governed by the endosomes-to-TGN retrieval network system for GLUT4 operating with retromers, golgin-97 and syntaxin 6, the housekeeping vesicle-trafficking machinery (Figures 4–8 and S3). Therefore, sortilin reduction in fully differentiated adipocytes under either siRNA-mediated (experimental) or ET-1–induced (pathological) conditions apparently disrupted the GLUT4 sorting process (Figure 3), possibly resulting in mistargeting of GLUT4, rendering it unable to reach the stationary GLUT4 storage compartment. Rescue of sortilin expression in siRNA-treated cells restored static GLUT4 behavior (Figure S2), indicating that sortilin-mediated proper sorting of GLUT4 to the stationary compartment plays a critical role in GLUT4 behavior and insulin-dependent glucose homeostasis.

It had long been widely believed that insulin resistance is caused by defects in insulin signaling (42), but severe defects in insulin-induced GLUT4 translocation were shown to be induced by independent or minor reductions of insulin signaling (8,43,44). Some of these defects could be related to down-regulation of sortilin expression (26,45), strongly suggesting that insulin resistance can occur via defects of not only insulin signaling itself but also those of sortilin-mediated GLUT4 sorting. In line with this notion, it was recently reported that a polymorphism at the chromosome 1p13 locus, which is strongly associated with both hypercholesterolemia and myocardial infarction alters hepatic sortilin expression (46), and that sortilin serves as a sorting receptor for apolipoprotein B100, an obligatory structural component of very low-density lipoprotein secreted from the liver (47). These observations indicate that proper actions of sortilin are critical for the complex regulation of intracellular sorting events that directly contribute to modulating systemic homeostasis. Thus, such 'sorting defects' have pivotal etiological roles in various late-onset diseases including type 2 diabetes, hypercholesterolemia and myocardial infarction.

We herein provide detailed mechanistic insights into sortilin actions that are mediated by recruiting GLUT4 to its putative anchoring sites via retromer-dependent endosomes-to-TGN retrieval through a mechanism involving golgin-97, a TGN-golgin (Figures 4–8). The crucial role of the retromer complex in this process is also confirmed by siRNA experiments showing that sortilin-mediated establishment of static GLUT4 behavior is significantly compromised in Vps29-depleted cells (Figure 4). Importantly, we also found that sortilin-mediated retrograde trafficking contributes to redistributing syntaxin 6 as well as Vti1a, both of which have been implicated in GLUT4 regulation (48,49), to the perinuclear region (Figure 8).

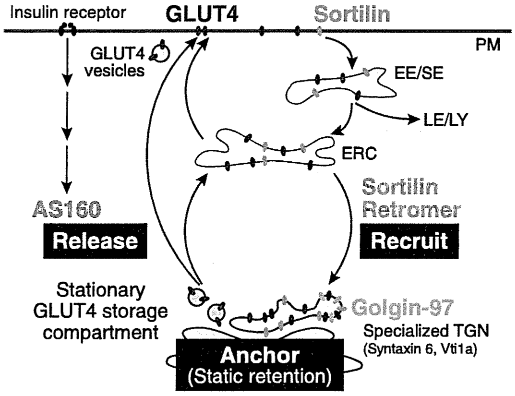

Figure 10: Schematic representation of the molecular basis of insulin-responsive GLUT4 trafficking systems in 3T3L1 adipocytes. After internalization from the plasma membrane, GLUT4 is sequestered from general recycling pathways involved in recycling of TfR, and recycled back to its stationary storage compartment(s) postulated to be derived from subdomains of the TGN. GLUT4 recruitment along this additional pathway from the endosomal recycling compartment (ERC) to the TGN is mediated by sortilin and retromers. Golgin-97, a TGN-golgin, appears to act as an intermediate transit point for the recruited GLUT4 en route to its putative anchoring sites. AS160/Tbc1d4 regulates the insulin-dependent liberation of GLUT4 from its storage compartments. EE/SE; early endosome/sorting endosome, LE/LY; late endosome/lysosome.

Together, these findings imply that sortilin mediates retrograde trafficking of certain TGN-resident t-SNARE proteins in addition to GLUT4, thereby perhaps consequently and cooperatively contributing to establishment of the fully functional TGN architecture that governs the GLUT4 'static retention' system in differentiated adipocytes. Malfunctions of sortilin as well as its regulation thereby disrupt the systematization of GLUT4 regulation, as manifested under certain pathophysiological conditions.

Although mechanistic details of sortilin-dependent redistribution of these SNARE proteins remain to be clarified, intraluminal interactions of single-spanning membrane proteins with GLUT4 in endosomes including sortilin, IRAP and LRP1 have been suggested to play roles in insulin-responsive GLUT4 vesicle formation (13,50,51). Unlike sortilin and GLUT4, both IRAP and LRP1 are expressed even in undifferentiated fibroblasts (13,51), though their contents increase upon differentiation along with sortilin emergence. We have also obtained data suggesting these interactions, i.e. siRNA-mediated knockdown of sortilin in adipocytes, to result in reduced IRAP contents (unpublished observation). In addition, concomitant decreases in syntaxin 6, sortilin and GLUT4 contents have reportedly been induced upon siRNA-mediated knockdown of Ubc9 in 3T3L1 adipocytes (52), due perhaps to the increased trafficking of these proteins into the lysosomal pathway (9,52). Therefore, it is plausible that up-regulated sortilin initiates these intraluminal interactions possibly in conjunction with their cytosolic interactions with adaptors including retromers, which are apparently required for proper GLUT4 sorting events, and contributes to the prevention of lysosomal degradation of GLUT4-containing cargos upon adipogenic differentiation (9). In any case, our data indicate that sortilin does not need to be persistently segregated (enriched) into the stationary GLUT4 storage compartment (Figure 5), but rather that sortilin retrieves GLUT4 (possibly assembling with IRAP and/or LRP1) from endosomes and then perhaps discharges GLUT4-containing cargo(s) after committing to a subdomain of TGN possessing golgin-97 (Figures 6–8). Consistent with this notion, sortilin does not redistribute to the plasma membrane in response to insulin in 3T3L1 adipocytes (53) (data not shown), while IRAP obligatorily serves and acts together with GLUT4 (13,41,54). Moreover, syntaxin 6 also reportedly translocates to the plasma membrane in response to insulin stimulation in adipocytes (16,48).

New key players identified herein as functioning in the GLUT4 regulatory system include TGN-golgins, especially golgin-97. Golgins are coiled-coil proteins mediating the architecture and function of the Golgi apparatus via their membrane tethering properties (55,56), and we indeed observed golgin-97 to be crucial for TGN retention of t-SNARE syntaxin 6 (Figure S3), as described in other cell types (32,33). At present, the possible involvement of golgin-245 remains uncertain since our present approach does not distinguish between GLUT4 in its *bona fide* static storage compartment and that mistargeted to a similar static, but irrelevant compartment (Figures 6 and 7). Thus, caution must be exercised in interpreting data regarding golgin-245 functions. However, it is increasingly apparent that TGN-golgins are required for tethering and fusion of recycling endosomes-derived retrograde transport vesicles to the TGN. Thus, our overall observations imply that golgin-97 regulates transient capture and fusion of sortilin-recruited GLUT4 or GLUT4-containing transport intermediates on the TGN and also suggest that golgin-97-localizing TGN serves as an important segregation point where only certain cargos including GLUT4, but not sortilin, can further proceed to their final destination, i.e. the stationary storage compartment. In this regard, since multiple studies have demonstrated that both the N- and the C-terminus of GLUT4 play important roles in its intracellular trafficking routes and destinations, with the C-terminus of GLUT4 being especially important for its perinuclear TGN accumulation (16,57–59), further studies are needed to clarify the interrelationships among these GLUT4 targeting sequences and the sortilin-mediated retrograde trafficking processes revealed by this investigation. In addition, substantial amounts of sortilin are detected in GLUT4-containing vesicles obtained by subcellular fractionation experiments (9,12,13). Our present data, therefore, suggest sortilin, but not GLUT4, to indeed be sequestered intracellularly *via* continuous release and recycling between the ERC and the TGN communicating with the stationary GLUT4 storage compartment. Thus, future studies are also warranted to clarify the regulatory mechanism(s) underlying assembly/disassembly of the GLUT4-containing protein complex with sortilin that occur as these proteins move along their functional trafficking pathways.

An important characteristic property of the TGN-golgins is binding with small GTPases including those of the Arl and Rab families (60,61). Adipose tissue-specific knockout of Arfrp1 GTPase, a member of the Arl family, in mice or knockdown of the protein in 3T3L1 adipocytes was recently demonstrated to alter GLUT4 trafficking and its increased localization at the plasma membrane (62). Thus, it is not unreasonable to speculate that the actions of Arfrp1 are mediated by TGN-golgins like golgin-97 and golgin-245, as this protein is required for TGN recruitment of these TGN-golgins (63,64). In addition to both TGN-golgins studied herein, mammalian cells express two additional TGN-golgins, GCC185 and GCC88 (65), localizing to a distinct subdomain of the TGN (66,67) with different Arl1-binding properties (68). Since these four TGN-golgins appear to regulate distinct, but somewhat redundant, retrograde pathways (32,69,70), the partial effect of golgin-97 knockdown on GLUT4 behavior (Figure 7) raises the possibility of the participation of other TGN-golgins in the retrieval process as well as the post-retrieval process required for development of stationary GLUT4 behavior and GLUT4 anchoring that apparently relies on Golgi apparatus architecture and function. Although we found that golgin-97 knockdown significantly affected both velocities and MSD (Figures 6 and 7, *red lines*), the both actions were only partial. This may be because GLUT4 molecules in these cells are probably mistargeted to compartments other than stationary anchoring sites in TGN including lysosomes. Therefore, the movements may reflect GLUT4 within mistargeted organelles such as lysosomes. This issue needs to be further clarified in a future study.

TGN-golgins reportedly have multiple binding sites for Rab proteins (71,72), and GLUT4-containing vesicles have several Rab proteins (73,74). We herein demonstrated that AS160, an insulin-regulated RabGAP inactivated by Akt-mediated phosphorylation, an activity which is related to insulin-responsive GLUT4 translocation (73–75), is required for insulin-responsive GLUT4 liberation from stationary storage compartments (8) (Figures 9 and S5). Although the mechanisms have yet to be elucidated in detail, overall observations suggest that Rab proteins might mediate actions between TGN-golgins and AS160. TGN-golgins and their regulatory small GTPases as well as AS160 may even form complex 'supra-molecular architectures' acting as frameworks for anchoring and liberation of GLUT4 in stationary storage compartments. It is also possible that AS160 contributes to further GLUT4 recruitment to the insulin-responsive compartment. We performed AS160 knockdown experiments in adipocytes and confirmed that endogenous AS160 has crucial a role in GLUT4 liberation in response to insulin stimulation in fully differentiated adipocytes (Figure S5B–E). In AS160-depleted adipocytes, we did not observe disappearance of static GLUT4 behavior in the basal state to a degree similar to that so readily detect in the sortilin-depleted adipocytes. However, we did detect very subtle but statistically significant alterations (mean velocities) in the basal behavior of GLUT4 molecules (Figure S5F,G). Biochemical studies have suggested that AS160 plays a role in basal retention of GLUT4 in adipocytes (74,76,77). Nevertheless basal surface amount of GLUT4 induced by the AS160 depletion appeared to be markedly lower than that under insulin-stimulated conditions (74,77). Therefore, AS160 may play a role in basal retention of GLUT4 (i.e. AS160 knockdown induces a minimal, perhaps reluctant, release of GLUT4 from retention). It is also possible that AS160 knockdown leads to mistargeting of GLUT4 to sites other than fully insulin-responsive compartments, and that this mistargeted GLUT4 slowly cycles between these incorrect destinations and the plasma membrane. Since our present analysis did not distinguish between GLUT4 in its static, but insulin-unresponsive, compartment endowed upon sortilin expression alone and that in its bona fide insulin-responsive compartment endowed upon sortilin plus AS160 expressions under quiescent basal conditions (Figure 9), further investigation is necessary to fully characterize these static GLUT4 compartments. Combining our technique with other approaches is anticipated to further understanding of how AS160 liberates GLUT4 from stationary storage compartments. In addition, it should be noted that other tethering factors localized to the Golgi cisternae, including p115 and golgin-160, might also take part in GLUT4 anchoring mechanisms (78,79).

Taking advantage of QD-labeling of surface-exposed myc-GLUT4, we selectively analyzed GLUT4 that had been recycled back from the plasma membrane, thereby highlighting the importance of the aforementioned sortilin-mediated retrograde trafficking to the TGN en route to insulin-responsive stationary GLUT4 storage compartments. Sortilin is known to regulate both anterograde and retrograde trafficking pathways by binding with cytoplasmic adaptors including GGAs and retromers (80). Previous work also demonstrated a GGA-dependent step to be involved in the entry of newly synthesized, but not recycled, GLUT4 into the insulin-responsive storage compartment (81). Thus, the mechanism regulating newly synthesized GLUT4 seems to be different and thus merits further study. However, the primary physiological actions of GLUT4 are probably mediated by recycled GLUT4 which has been exposed to the plasma membrane at least once, since GLUT4 is a long-lived protein (~50 h) (82) and is likely to repeatedly cycle between the plasma membrane and storage compartment during its lifetime in response to insulin after each meal.

Finally, myc-GLUT4 translocation assays fully support our notion that both sortilin and AS160 are essential for generating the insulin-responsive GLUT4 translocation system (data not shown), although previous reports have suggested sortlin alone to be sufficient for producing the insulin-responsive GLUT4 translocation (9,50). In the present study, we transiently expressed sortilin and/or AS160 in naive 3T3L1 fibroblasts that do not express any of these proteins (Figures 2A and S5A), but previous studies have used fibroblast clones constitutively expressing exogenous sortilin (9,50). Since we have reported that exogenous sortilin expression could stimulate cellular differentiation (25), prolonged sortilin expression might alter the cellular differentiation status that could be a reason for this apparent discrepancy.

In summary, insulin-responsive GLUT4 trafficking systems are governed by the highly orchestrated actions of sortilin, retromers, TGN-golgins and AS160. These complex interactions rely on the TGN which develops upon adipogenic differentiation (Figure 10). Various proteins, including the vasopressin-sensitive water channel aquaporin 2, cycle between the TGN and endosomes (83), in addition to GLUT4. Thus, it is possible that similar developmental mechanisms play roles in stimulus-dependent translocations in various cell types. Further elucidation of these mechanisms employing our nanometrological approach may provide new insights into the fundamentals of intracellular trafficking as well as the pathophysiological mechanisms underlying various diseases.

Materials and Methods

Plasmids and siRNAs

Expression vector containing cDNAs fused to HaloTag was purchased from Promega. The full-length cDNA encoding the cation-independent mannose 6-phosphate receptor was ligated into pEGFP-N3 at the EcoRI site. Human sortilin cDNA was ligated into pEYFP-N1 at the XhoI site (25). All mutations were generated by polymerase chain reaction-based site-directed mutagenesis and confirmed by sequencing (PRISM 3130, Applied Biosystems). siRNAs were designed and synthesized by Nippon EGT or Tomy Digital Biology.

Antibodies

The following antibodies were used: Actin (Sigma), Akt (Cell Signaling Technology), phosphorylated Akt (Ser473, Cell Signaling Technology), AS160 (Upstate Biotechnology for western blotting, Abcam for immunofluorescence), Golgin-245 (Santa Cruz Biotechnology), Golgin-97 (Abcam), myc (Santa Cruz Biotechnology), Sortilin (Abcam), Syntaxin 6 (Cell Signaling Technology), Vps29 (Abnova), Vti1a (BD Transduction Laboratories) and Alexa Fluor-conjugated secondary antibodies against the corresponding primary antibodies (Invitrogen).

Cells and transfection

3T3L1 fibroblasts stably expressing myc-GLUT4-ECFP were maintained and differentiated into adipocytes in a glass-bottomed recording chamber (thickness, 0.15–0.18 mm; Matsunami-glass) or a 6-well culture plate. In some experiments, differentiated cells (day 6) were re-plated onto glass-bottomed recording chambers and further cultured for 1–2 additional days for observation. We found no significant differences in GLUT4 movement between the culture conditions. Fibroblasts were transfected with either Lipofectamine LTX + PLUS (Invitrogen) or Lipofectamine 2000 (Invitrogen) with 1 µg plasmid DNA and/or 75–250 pmol siRNA according to the manufacturer's instructions. Electroporation into adipocytes was carried out as previously described (84). In brief, the cells were put into suspension by mild trypsinization and electroporated with 50–200 µg plasmid DNA and/or 1–2 nmol siRNA under low-voltage conditions (160 V, 950 µF). Some experiments were performed in WT 3T3L1 fibroblasts and adipocytes transiently expressing myc-GLUT4-EGFP. Western blotting was performed as previously described (84). In-gel fluorescence detection of sortilin/WT-EYFP was performed with a PharosFX Molecular Imager (BioRad). Excitation was at 488 nm, and the fluorescence was observed through a 530-nm bandpass filter.

QD-labeling of myc-GLUT4-ECFP or TfR

Labeling of myc-GLUT4-ECFP with QD was performed with the QD-conjugated Fab fragment of anti-myc antibody. The QD-conjugated antibody was prepared with a QD antibody conjugation kit (Invitrogen), and the final concentration of the QD-conjugated antibody was determined by optical density at the specified wavelength according to the manufacturer's instructions. For labeling, the cells were serum-starved and stimulated with 10 nM insulin in the presence of 1.5 nM QD-conjugated antibodies for 1 h. The cells were then extensively washed to remove excess insulin and unbound QD-labeled antibodies, followed by an additional incubation for 3 h. Conjugation of TfR with QD was performed using QD-conjugated transferrin. The QD-conjugated transferrin was prepared with transferrin–biotin and streptavidin–QD (Invitrogen) in the presence of an excess (100×) of the amount of biotin needed to achieve a single transferrin per QD (8). For labeling, adipocytes over-expressing TfR or fibroblasts were treated with the transferrin–QD conjugates for 15 min, and images were acquired for up to 30 min. We utilized several QDs having different fluorescent wavelengths for these experiments, and found no significant differences among them in behavioral characteristics.

Single-particle tracking and movement analysis

Single-molecule imaging was performed with an inverted microscope (IX71, Olympus) equipped with an electron-multiplying charge-coupled device camera (iXon 887, Andor Technology), a Nipkow disk confocal unit (CSU10, Yokogawa), and an oil-immersion objective lens (UPLSAPO100xO, Numerical Aperture of 1.40, Olympus) at ~30°C. Excitation was performed at 488 or 532 nm with solid-state lasers (Spectra-Physics). In these experiments, expression of sortilin-EYFP and HaloTag-AS160 was confirmed by EYFP fluorescence and by staining the cells with HaloTag Ligand TMR (Promega), respectively. Single-particle tracking and MSD calculations were performed with G-Count and G-Track software with a two-dimensional Gaussian fitting mode (G-Angstrom). We tracked each particle which was successfully fitted within an 8 × 8 pixel region-of-interest for at least 30 frames. When the signal in a frame was lost because of blinking, no fitting was performed until reappearance of the bright spot. When a bright spot did not reappear within 10 frames, tracking was aborted. We typically tracked 50–150 particles per cell, and obtained the images in at least three independent experiments. We evaluated movements employing a set of four analytical schemes; (i) velocity distributions, (ii) mean velocities, (ii) MSD curves and (iv) diffusion coefficient maps. The velocities for individual particle movements were calculated by linear fit of the displacement during four frames, as previously described (8). Mean velocities and frequency distributions were first calculated in a cell, and then averaged among cells under the same treatment conditions. Diffusion coefficients of individual molecules were estimated by fitting the first 10 points of the MSD curves versus time with

$$\mathrm{MSD}(t) = 4D_{10}t + C \qquad (1)$$

where t, D_{10} and C are time, the diffusion coefficient of the first 10 points and instrumental noise, respectively. The D_{10} value was calculated and D_{10} maps were constructed using a custom-written program based on LabVIEW and Vision (National Instruments).

Immunofluorescence and co-localization analysis

Immunofluorescence was performed as previously described (84). For labeling of internalized GLUT4, serum-starved cells were treated with 10 nM insulin in the presence of 4 µg/mL anti-myc immunoglobulin G (IgG) mouse monoclonal antibodies for 1 h. After being washed for 3 h, the cells were fixed, permeabilized and stained with Alexa Fluor-conjugated anti-mouse IgG. For double staining of vti1a and internalized GLUT4, we used a Zenon mouse IgG1 labeling kit (Invitrogen) for preparing Alexa Fluor-labeled anti-vti1a antibodies. The imaging was performed with an inverted microscope (IX81, Olympus) equipped with a laser scanner (FV1000, Olympus) and an oil-immersion objective lens (PlanApo 60×, Numerical Aperture of 1.40, Olympus). Fluorescence of ECFP, EGFP, EYFP, Alexa555/Cy3 and Alexa647 was excited at 458, 488, 515, 543 and 633 nm, and detected at 480–495, 505–525, 533–565, 560–620 and >650 nm, respectively, by a sequential acquisition mode. The recorded 12-bit TIFF images were converted into 16-bit data and processed with ImageJ software (NIH). Background fluorescence was measured within the cell-free area adjacent to the cell of interest, and its mean+3SD value was subtracted from the entire image. Quantitative co-localization analysis was performed with Intensity Correlation Analysis plug-in of ImageJ (85).

Myc-GLUT4 translocation assay

Myc-GLUT4 translocation assays were performed in 3T3L1 fibroblasts expressing myc-GLUT4-EGFP in the presence or absence of HA-sortilin and HaloTag-AS160. Serum-starved cells were insulin-stimulated (100 nM, 20 min), washed with ice-cold PBS, and then fixed with 1% paraformaldehyde. Surface myc-GLUT4-EGFP were labeled with anti-myc antibodies and subsequently with Alexa555-anti mouse IgG. The fluorescence of EGFP (total myc-GLUT4-EGFP) and Alexa555 (surface myc-GLUT4-EGFP) was acquired, and the background fluorescence of each fluorescent image was corrected. Based on these images, the ratio of fluorescence intensity ($F_{\mathrm{Alexa555}}/F_{\mathrm{EGFP}}$) was calculated.

Statistical analysis

Statistical analysis was performed with the Mann–Whitney *U* test unless otherwise indicated, and *p* values <0.05 were considered to be statistically significant.

Acknowledgments

The authors thank Fumie Wagatsuma and Natsumi Emoto for their excellent technical assistance. This study was supported by grants from the Ministry of Education, Science, Sports and Culture of Japan (#22590969 and #20001007) and the New Energy and Industrial Technology Development Organization (NEDO). This study was also partially supported by Banyu Life Science Foundation International and Takeda Science Foundation. H. H. is a Research Fellow of the Japan Society for the Promotion of Science.

Supporting Information

Additional Supporting Information may be found in the online version of this article:

Figure S1: Behavioral differences between undifferentiated fibroblasts and differentiated adipocytes. A) Mean MSD curves in 3T3L1 fibroblasts (*black*) and adipocytes (*red*). MSD values were calculated from the same data shown in Figure 1C. Data are presented as mean ± SEM. B and C) Velocity distributions of the movement of GLUT4 (*red*) and TfR (*black*) in adipocytes (B) and fibroblasts (C). The mean velocities (±SD) were as follows. Adipocytes, 0.31 ± 0.03 µm/s (GLUT4, $n = 11$) and 0.47 ± 0.06 µm/s (TfR, $n = 7$, $p < 0.001$). Fibroblasts, 0.86 ± 0.34 µm/s(GLUT4, $n = 17$) and 0.88 ± 0.19 µm/s (TfR, $n = 10$, $p = 0.47$). D) Mean MSD curves of GLUT4 in control fibroblasts (black) or fibroblasts expressing sortilin/WT-EYFP (red). MSD values were calculated from the same data shown in Figure 2B. Data are presented as mean ± SEM.

Figure S2: Effects of sortilin knockdown on GLUT4 movement and insulin-induced Akt phosphorylation in adipocytes. A and B) Velocity distributions (A) and mean MSD curves (B) of GLUT4 in differentiated adipocytes electroporated with sortilin siRNA (*red*), sortilin siRNA + siRNA-resistant sortilin/WT-EYFP (*blue*) and scrambled siRNA (*black*). The mean velocities (±SD) were 0.36 ± 0.04 µm/s (scrambled siRNA, $n = 16$), 0.51 ± 0.11 µm/s (sortilin siRNA, $n = 21$, $p < 0.01$), and 0.43 ± 0.02 µm/s (sortilin siRNA + sortilin/WT-EYFP, $n = 10$, $p = 0.25$). Statistical analysis was performed with Dunnett's multiple comparison versus scrambled siRNA. In (B), data are presented as mean ± SEM. C) Western blotting of endogenous sortilin and actin, and fluorescence detection of sortilin/WT-EYFP in adipocytes electroporated with indicated siRNA and plasmid. D) Western blotting of sortilin, phosphorylated Akt (Ser^{473}) and total Akt in adipocytes electroporated with sortilin or scrambled siRNA. The cells were treated with the indicated concentrations of insulin for 30 min.

Figure S3: Effects of TGN-golgins knockdown on localization of syntaxin 6 in adipocytes. A) Immunofluorescent images of golgin-97 and syntaxin 6 in adipocytes electroporated with control (top) or golgin-97 (bottom) siRNA. Asterisk denotes a cell apparently without golgin-97 knockdown. B) Western blotting of golgin-97, sortilin and actin in adipocytes electroporated with control or golgin-97 siRNA. C) Immunofluorescent images of golgin-245 and syntaxin 6 in adipocytes electroporated with control (top) or golgin-245 (bottom) siRNA.

Figure S4: AS160 contributes to insulin-responsive liberation of static GLUT4. A) Western blotting of AS160 during differentiation. B–D) Mean MSD curves of GLUT4 movement in fibroblasts expressing sortilin/WT-EYFP (B), sortilin/WT-EYFP + HaloTag-AS160 (C), and HaloTag-AS160 (D) before (*black*) or after (*red*) insulin stimulation (100 nM, 30 min). MSD values were calculated from the same data shown in Figure 6A,C,E. Data are presented as mean ± SEM. E–H) Velocity distributions (E and G) and diffusion coefficient maps (F and H) of GLUT4 movement in fibroblasts expressing sortilin/WT-EYFP + HaloTag-AS160 pretreated with 100 nM wortmannin for 30 min (E and F) and sortilin/WT-EYFP + T642A mutant of HaloTag-AS160 (G and H) before or after insulin stimulation (100 nM, 30 min). The mean velocities (±SD) were as follows. Sortilin/WT-EYFP + HaloTag-AS160 + Wortmannin ($n = 3$); basal: 0.49 ± 0.10 µm/s, insulin: 0.47 ± 0.01 µm/s ($p = 0.66$), sortilin/WT-EYFP + T642A mutant of HaloTag-AS160 ($n = 4$); basal: 0.46 ± 0.01 µm/s, insulin: 0.49 ± 0.05 µm/s ($p = 1$).

Figure S5: Effects of AS160 knockdown on GLUT4 behavior in adipocytes. A) Fluorescent image of myc-GLUT4-EGFP (left) and immunofluorescent image of AS160 (right) in adipocytes electroporated with both myc-GLUT4-EGFP and AS160 siRNA. B–E) Insulin actions in adipocytes electroporated with control (B and C) or AS160 (D and E) siRNA. Velocity distributions (B and D) and mean MSD curves (C and E) before (*black*) and after (*red*) insulin stimulation (100 nM, 30 min) are shown. The mean velocities (±SD) are as follows: Control ($n = 6$), 0.36 ± 0.04 µm/s (basal) and 0.59 ± 0.11 µm/s (insulin, $p < 0.01$). AS160 siRNA ($n = 6$), 0.41 ± 0.02 µm/s (basal) and 0.48 ± 0.04 µm/s (insulin, $p < 0.05$). F and G) Velocity distributions (F) and mean MSD curves (G) of GLUT4 in adipocytes electroporated with control (*black*) or AS160 (*blue*) siRNA plus mycGLUT4EGFP. The mean velocities (±SD) were 0.38 ± 0.03 µm/s (control, $n = 6$) and 0.43 ± 0.02 µm/s (AS160 siRNA, $n = 10$, $p < 0.05$). In (G), data are presented as mean ± SEM.

References

1. Nielsen S, Chou CL, Marples D, Christensen EI, Kishore BK, Knepper MA. Vasopressin increases water permeability of kidney collecting duct by inducing translocation of aquaporin-CD water channels to plasma membrane. Proc Natl Acad Sci U S A 1995;92:1013–1017.
2. Kanzaki M, Zhang YQ, Mashima H, Li L, Shibata H, Kojima I. Translocation of a calcium-permeable cation channel induced by insulin-like growth factor-I. Nat Cell Biol 1999;1:165–170.